

7N-46-CR
139629
P-58

Semiannual Status Report

NASA-Ames Cooperative Agreement Number NCC 2-662

MODELLING ATMOSPHERIC SCATTERERS USING SPACECRAFT OBSERVATIONS

For the period April 1 through September 30, 1992

Submitted to

Dr. James B. Pollack, Technical Officer
Theoretical Studies Branch, 245-3
National Aeronautics and Space Administration
Ames Research Center
Moffett Field, California 94035

Prepared by

Dr. Kathy A. Rages, Principal Investigator
Space Physics Research Institute
572 Hyannis Drive
Sunnyvale, California 94087-1315
(408) 736-9705

(NASA-CR-191688) MODELLING
ATMOSPHERIC SCATTERERS USING
SPACECRAFT OBSERVATIONS Semiannual
Status Report, 1 Apr. - 30 Sep.
1992 (Space Physics Research
Inst.) 58 p

N93-71152

Unclass

29/46 0139629

Progress Report

Work this period has focussed on the reexamination of high-resolution Voyager images of the limb of Titan.

The first analysis of a high phase angle Voyager image of Titan (FDS# 43996.24) was carried out in 1982-83 with the results published in Icarus (Rages and Pollack 1983). During the past six months this image has been reexamined with improved computer codes for inverting radial intensity profiles to yield vertical atmospheric extinction profiles. This image was taken at a solar phase angle of 155° and scattered light is clearly visible around the entire circumference of Titan. (About 90° of the circumference is chopped off at the top of the frame.) Extinction profiles have been generated at 5° intervals over the entire visible limb, together with values for the albedo-weighted single scattering phase function at 25° scattering angle. The latitudes of the derived extinction profiles range from 75°N to 80°S . Titan's detached haze layer is visible everywhere south of about 60°N , and the enhanced extinction characterizing the north polar hood is seen north of this latitude.

An additional Titan image (FDS# 43990.43) has also been analyzed using the improved limb inversion code. This image was taken at a solar phase angle of 140° and has a spatial resolution about 50% higher than the 155° image. Only the bright limb is visible in this image, corresponding to latitudes between 25°S and 72°N . Figures 1-3 show the extinction profiles derived from each of these two images, for latitudes of 23°S , 30°N , and 70°N . As expected, the extinction profiles derived for similar locations in the two different images are very nearly the same. The slight difference between the altitudes of the detached haze layer in the two profiles in Figs. 1 and 2 can be explained entirely by a minor discrepancy in the registration of the two images.

Figures 4 and 5 show the altitude at which the haze optical depth reaches 0.01 in each of the vertical extinction profiles of the 155° and 140° images, respectively. This altitude shows a measurable variation with latitude in the 155° image, lying about 35 km lower over the poles than over the equator (solid line). Although the 140° image doesn't show enough of the limb to pin down the ratio of polar to equatorial radius with any great accuracy, the 0.01 optical depth level in Fig. 5 is also fit better by an ellipsoid than by a sphere. The best fitting sphere in both images is also shown (dashed line). END

One of the improvements made to the limb inversion code was to carry out singular value decomposition of the design matrix instead of inverting the normal equation matrix to find the increments in the vertical extinctions most likely to minimize the sum of the squared differences between the observed and calculated specific intensities. This resulted in much more rapid convergence and a reduction of an order of magnitude in the CPU time required. A detailed comparison of the two methods of handling nonlinear least squares optimization has been written up for the use of others in the Theoretical Studies branch who may wish to apply singular value decomposition to their own least squares fitting problems. A copy of the write-up is included as Appendix A.

The analysis of high phase angle Voyager images of Triton carried out previously is due to appear in the October issue of Icarus. A copy of the final version of the paper, "Voyager Imaging of Triton's Clouds and Hazes" by K. Rages and J. B. Pollack, is included as Appendix B.

References

- Rages, K., and J. B. Pollack (1983). "Vertical distribution of scattering hazes in Titan's upper atmosphere." Icarus 55, 50-62.

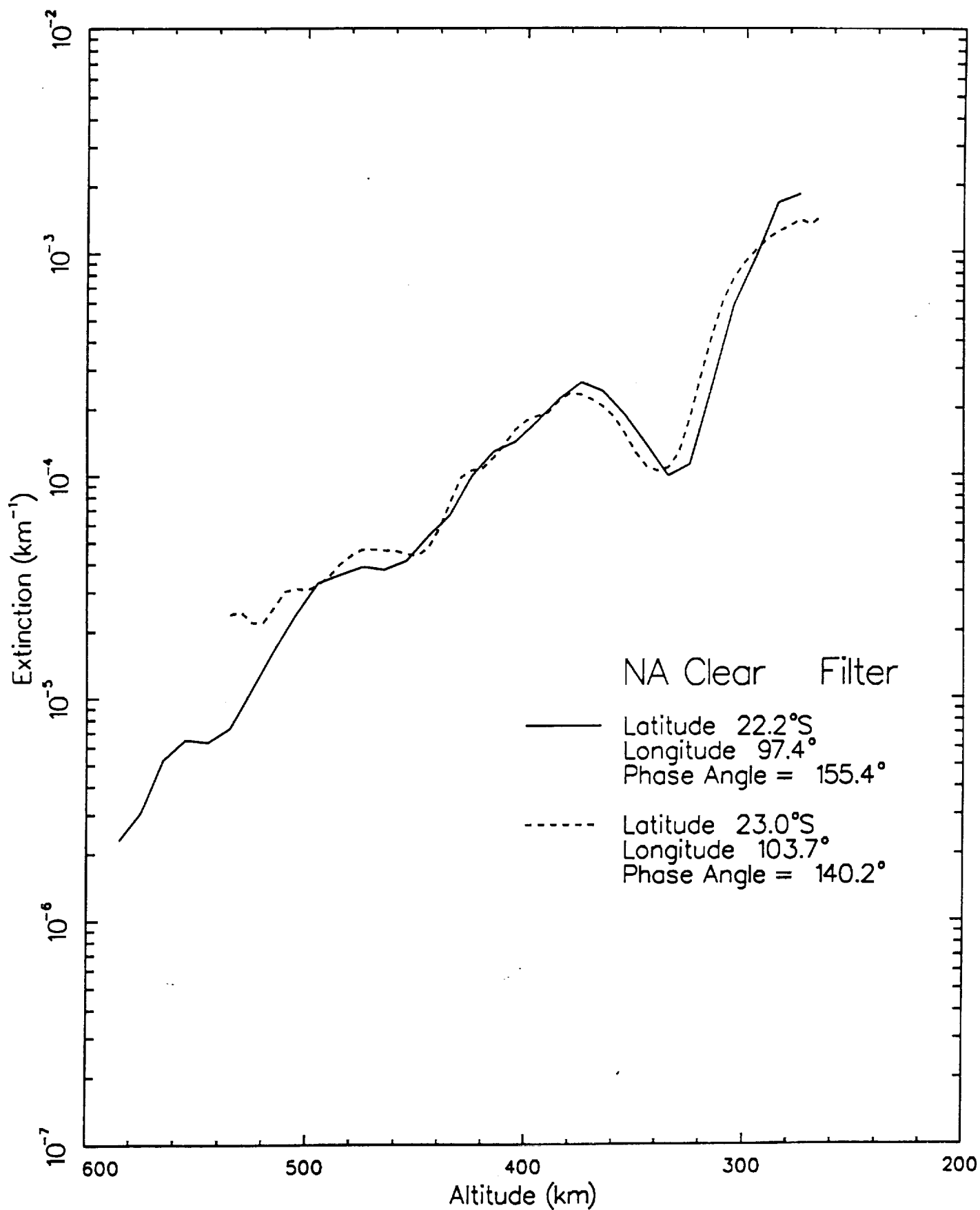


Figure 1.

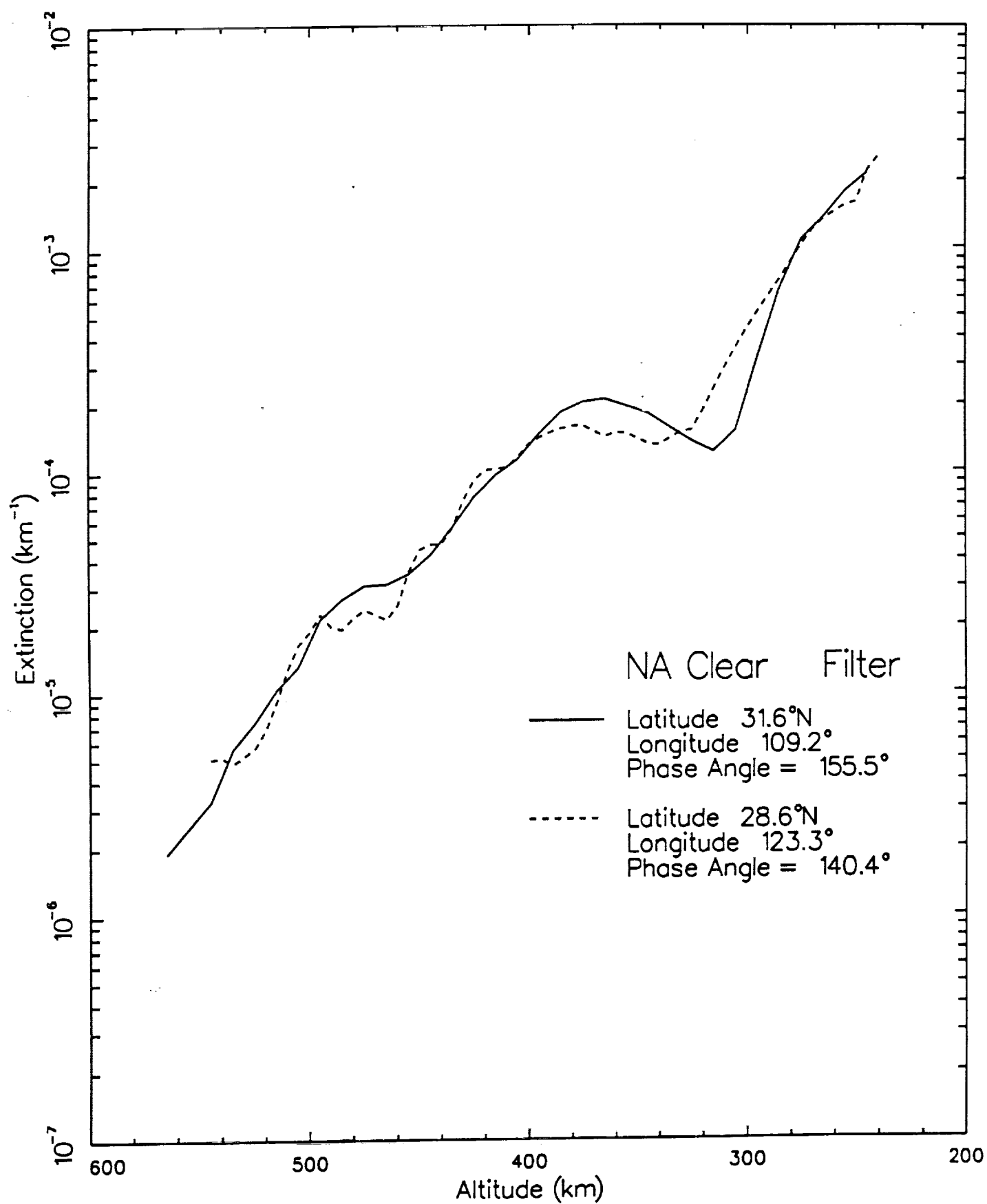


Figure 2.

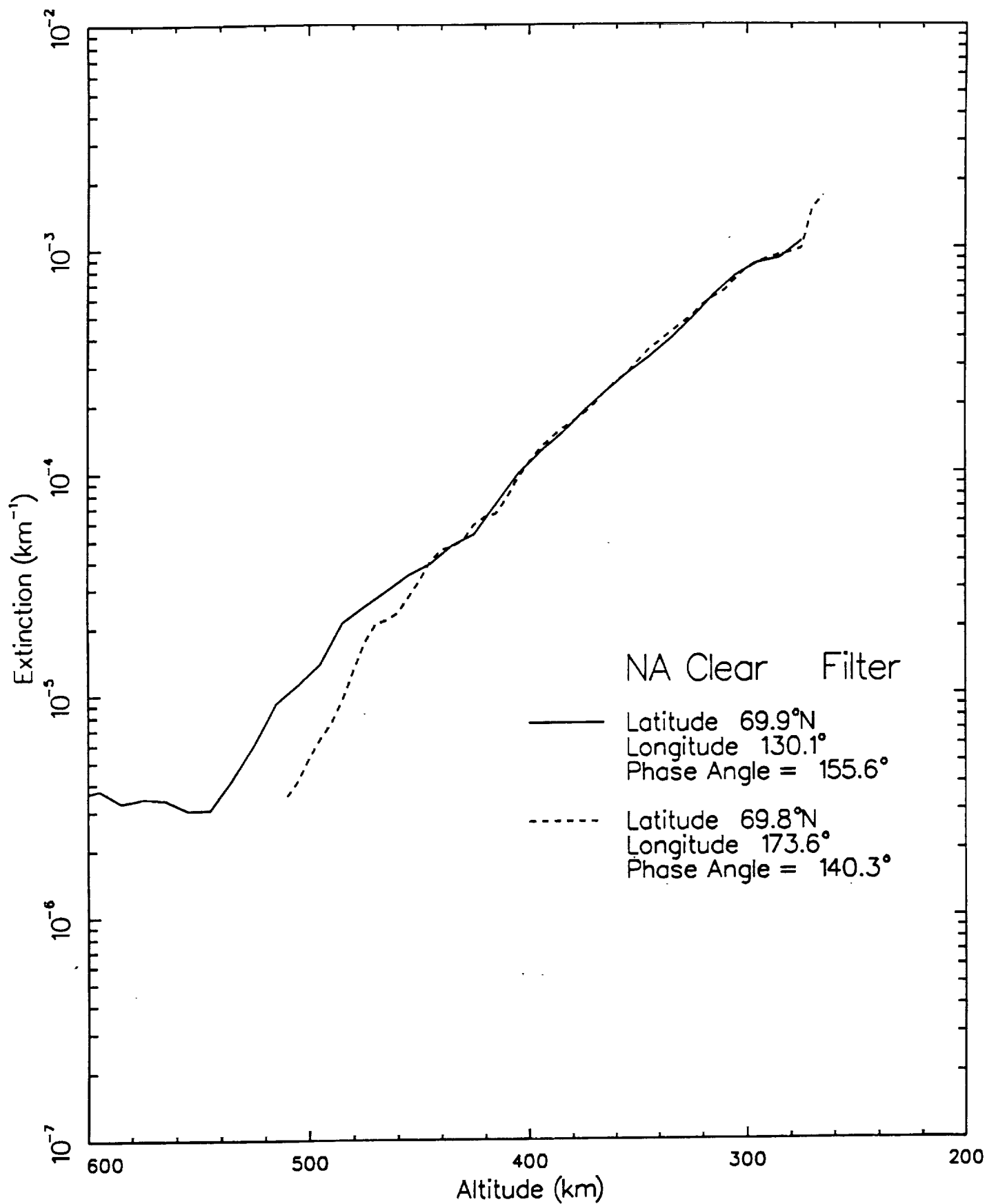


Figure 3.

Titan --- $\tau = 0.01$ Radii
 Phase Angle = 155°

—— $r_{\text{pol}} / r_{\text{eq}} = 0.9885$ - - - - $r_{\text{pol}} / r_{\text{eq}} = 1$

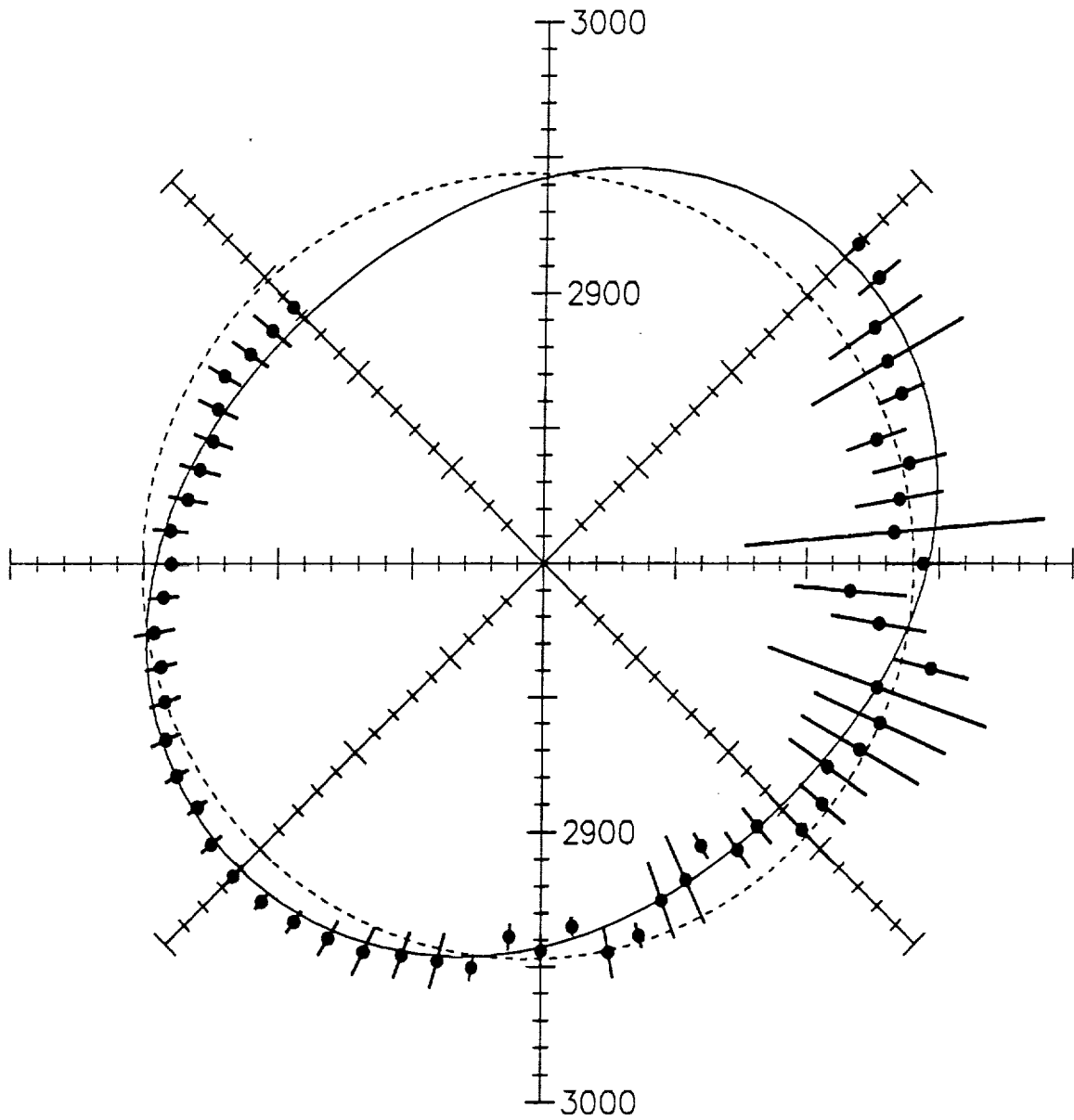


Figure 4.

Titan -- $\tau = 0.01$ Radii
 Phase Angle = 140°

— $r_{\text{pol}} / r_{\text{eq}} = 0.9885$ - - - $r_{\text{pol}} / r_{\text{eq}} = 1$

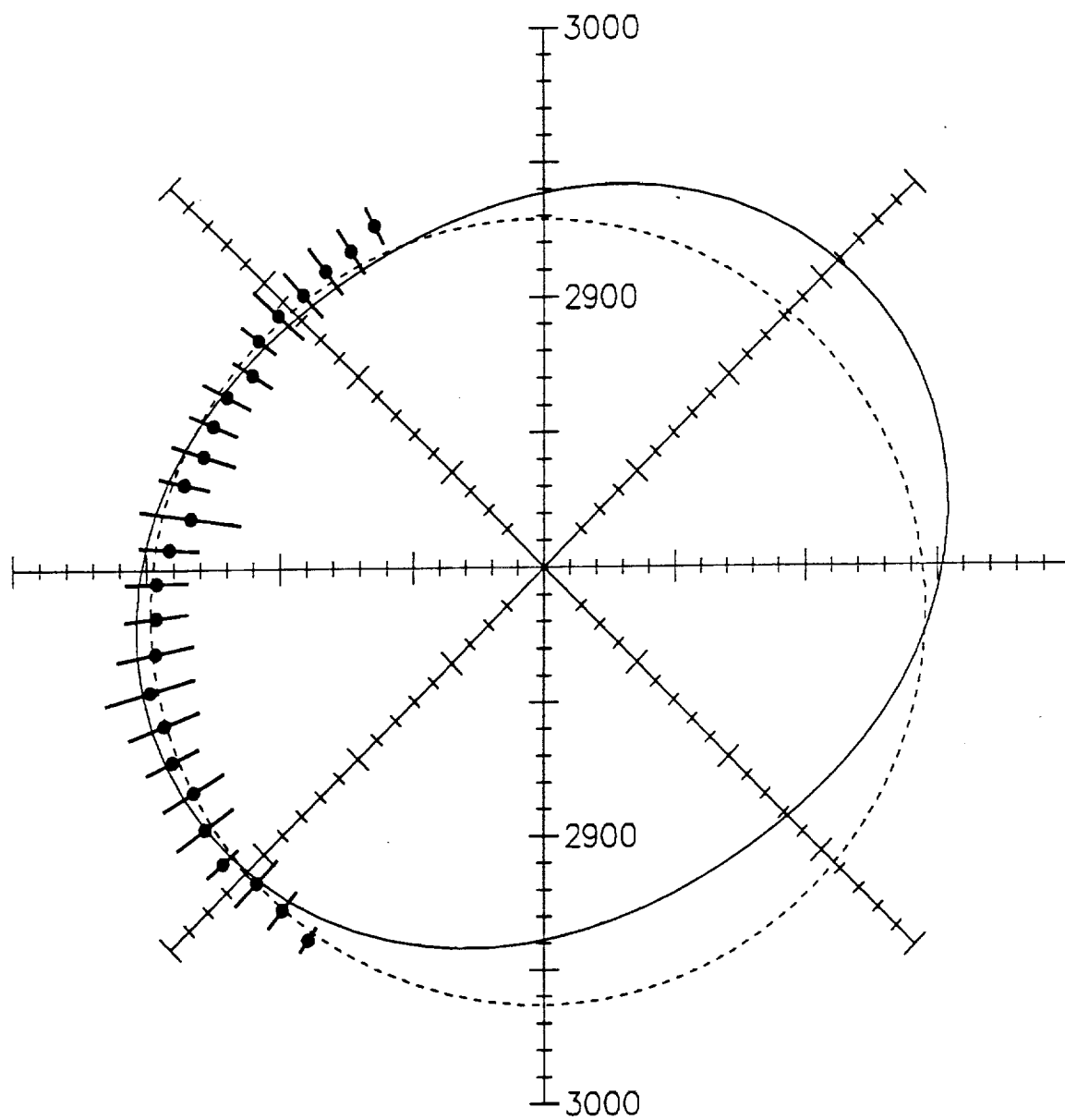


Figure 5.

Singular value decomposition as an exorcist's tool in least squares optimization

by

Kathy Rages

What is nonlinear least squares optimization?

In a least squares fit we are trying to find the minimum in χ^2 :

$$\chi^2 = \sum_N \left[y_o - y_c(x_1, x_2, \dots; p_1, p_2, \dots) \right]^2 w_o \quad (1)$$

N is the number of data points

y_o is the observed value at each data point

y_c is the calculated value at each data point (as a function of x 's and p 's)

x 's are independent variables which are not free parameters

p 's are free parameters

w_o is the weight given to each data point

The only difference between linear least squares and nonlinear least squares is that in the nonlinear case the derivative of y_c with respect to the p 's is a function of the p 's. This means that the optimum value of the p 's can only be found by iteration. (In the linear case you calculate the basis functions, which depend only on the x 's, and then find the optimum p values in one fell swoop.) Chapter 14 (particularly 14.1-14.5) of Numerical Recipes (Press *et al.*, 1989) is where I learned most of what I know about least squares. Most of the algorithms given there are for linear least squares problems, but the general discussion applies to all least squares optimization.

What is singular value decomposition?

Chapters 2.9 and 14.3 of Numerical Recipes are where I learned all that I know about singular value decomposition (SVD), and I really, *really*, really urge you to read these.

Briefly, it appears that any real $N \times M$ matrix A , where $N \geq M$, can be written as the product of an $N \times M$ matrix U , an $M \times M$ diagonal matrix S , and the transpose of an $M \times M$ matrix V

$$\begin{pmatrix} \mathbf{A} \end{pmatrix} = \begin{pmatrix} \mathbf{U} \end{pmatrix} \begin{pmatrix} s_1 & & \\ & s_2 & \\ & & \ddots \\ & & & s_m \end{pmatrix} \begin{pmatrix} \mathbf{V}^T \end{pmatrix} \quad (2)$$

I can hear you now saying “Big fat hairy deal. I always simplify my life by turning every matrix I meet into three other matrices”. The fun comes from the fact that \mathbf{V} is orthogonal and \mathbf{U} is column-orthogonal.

$$\sum_{k=1}^M V_{ik} V_{jk} = \sum_{k=1}^M V_{ki} V_{kj} = \delta_{ij}$$

$$\sum_{k=1}^N U_{ki} U_{kj} = \delta_{ij} \quad (3)$$

$$\delta_{ij} = 1 \quad i=j$$

$$=0 \quad \text{otherwise}$$

Almost all the information about the magnitude of the elements in \mathbf{A} is concentrated in the N diagonal terms of \mathbf{S} , which are always positive or zero, and are called the singular values. The *columns* of \mathbf{V} are called (by me, anyway) the associated singular vectors. Whatever you call them, they’re significant, as we shall see.

Given the relations in Eq. 3, and the fact that all non-diagonal terms of \mathbf{S} are zero, it is left as an exercise for the reader to show that, if \mathbf{A} in Eq. 2 is a square matrix ($M=N$)

$$\mathbf{A}^{-1} = \mathbf{V} \cdot [\text{diag } (1/s_i)] \cdot \mathbf{U}^T \quad (4)$$

so once you’ve done the SVD of a matrix, you’ve also done most of the work toward finding its inverse.

Why do we care?

The usual way of handling a least squares problem is through inversion of the normal equation matrix \mathbf{C} . If the $M \times M$ matrix \mathbf{C} and the length- M vector \vec{F} are defined by

$$c_{mj} = \sum_{n=1}^N w_{on} \frac{dy_{cn}}{dp_m} \frac{dy_{cn}}{dp_j} \quad (5)$$

$$f_m = \sum_{n=1}^N w_{on} (y_c - y_o)_n \frac{dy_{cn}}{dp_m} \quad (6)$$

where M is the number of free parameters, then the change in the parameter vector \mathbf{P} is given by

$$d\mathbf{P} = \mathbf{C}^{-1} \vec{F} \quad (7)$$

The problem with this is that, depressingly often, \mathbf{C} is ill-conditioned if not downright singular. This indicates that there is some linear combination of the p_m 's which has little or no effect on χ^2 . Operationally, it leads to large and usually spurious values for $d\mathbf{P}$ and a general reluctance to converge. Enter SVD.

If \mathbf{C} is singular, one or more of its singular values (the s_m 's) will be zero. If \mathbf{C} is ill-conditioned the ratio of the largest and smallest s_m 's will be large. This is something that lends itself to ready inspection, before matrix inversion is even begun.

Actually, in least squares problems SVD is applied not to the normal equation matrix, but to the entire design matrix. (This is the only real disadvantage I can see to SVD vs. the usual method. You have to make room for an $N \times M$ matrix instead of an $M \times M$ matrix. If you have a lot of data points, this can add up to a *lot* of room.)

Define the $N \times M$ matrix \mathbf{A} and a length- N vector \vec{B} by

$$a_{nm} = w_{on} \frac{dy_{cn}}{dp_m} \quad (8)$$

$$b_n = w_{on} (y_c - y_o)_n \quad (9)$$

where N is the number of data points and M is the number of free parameters. Do SVD on \mathbf{A} . If there are one or more linear combinations of p_m 's that have little or no effect on χ^2 , one or more of the s_m 's will be zero, or much smaller than the largest s_m . The linear combination of free parameters responsible for this state of affairs will be given by the corresponding singular vector $\mathbf{V}_{(m)}$ (the *column* of \mathbf{V} having the same index as the small or zero s_m). The change in the parameter vector \mathbf{P} is now

$$d\mathbf{P} = \mathbf{V} \cdot [\text{diag } (1/s_m)] \cdot \mathbf{U}^T \cdot \vec{B} \quad (10)$$

Note the similarity to what you would get if you substituted Eq. 4 for the inverse matrix in Eq. 7. Another way to write Eq. 10, which emphasizes the role of the singular vectors, is

$$d\mathbf{P} = \sum_{m=1}^M \left(\mathbf{U}_{(m)} \cdot \vec{B} / s_m \right) \mathbf{V}_{(m)} \quad (11)$$

where $\mathbf{U}_{(m)}$ is the m^{th} column of \mathbf{U} .

And now you ask "How does this help us, since we're still dividing by those pesky small-or-zero s_m 's?". The answer is simple, even though it sounds ridiculous. If a particular s_m is too small for comfort, ignore that term. In effect, set $1/0 = 0$. It's magic. It works. Actually what happens is that any linear combination of free parameters ($\mathbf{V}_{(m)}$) that is ill determined (or undetermined) by the data is simply ignored, leaving us free to pin down the relationships among the free parameters that the data actually have something useful to tell us about.

Note: in the usual approach to the least squares problem, the weights w_o are generally defined by $1/\sigma_o^2$, where σ_o is the error bar on y_o . For SVD, w_o for each data point should be defined by $1/\sigma_o$.

Nitty-gritty

For the actual dirty work I use the **Imsl** routine **Lsvrr** on the Cray, or **Dlsvrr** on the Vaxes (because I just don't trust 32-bit accuracy for these least squares problems). The subroutine call is

```

      I   I   I   I   I   I   O   O   O   I   O   I
call Dlsvrr( ndp, ncf, A, lda, ipath, tol, irank, s, U, ldu, V, ldv )

```

where input arguments are marked I and output arguments are marked O.

ndp is the number of rows in A (= # of data points)

ncf is the number of columns in A (= # of free parameters)

A is the design matrix defined in Eq. 8

lda is the leading dimension of A as it occurs in the DIMENSION statement

ipath is a control variable which I set to 21. Read the manual.

`tol` is the tolerance used to determine `irank`. There are details. Read the manual. I used `1.e-10` in the accompanying example.

`irank` is the number of singular values the computer thinks are significantly different from zero, based on the value of `tol` you gave it.

`s` is a vector of length `ncf` containing the singular values

`U` is `U` from Eq. 2. `U` and `A` can be the same matrix in the calling statement, in which case `A` gets overwritten.

`ldu` is the leading dimension of `U` as it occurs in the `DIMENSION` statement

`v` is V^T from Eq. 2

`ldv` is the leading dimension of `V` as it occurs in the `DIMENSION` statement

Note: **Imsl 1.1** sets a default work area size of 5000. If you need more you will have to designate enough work area before calling `Lsvrr`. Judging by the notes on **Imsl 2.0** which just appeared on eagle today (9-15-92), the new version will take care of this automatically.

You change the work space allocation in version 1.1 by placing the following statements in your program.

```
C
C Work area for IMSL singular value decomposition
C
C     parameter( nwrk = ndp * ( ncf + 2 ) + ncf ) ! work area required
C     common /worksp/ rwksp(nwrk)
C
C Increase available work space for IMSL Lsvrr
C
C     call lwkin( nwrk )
```

A personal testimonial...

I have recently converted a program which inverts limb scans of planetary atmospheres to give atmospheric extinction as a function of altitude, to use singular value decomposition. In this case the y_o 's are measurements of specific intensity (I/F) vs. altitude, and the p 's are the atmospheric extinction (in km^{-1}) at a number of altitudes. Because the atmosphere must be treated as a spherical shell rather than a plane, the function describing I/F in terms of the extinction is very complicated, and nonlinear.

Previously, I was using the usual matrix inversion procedure to do this, and I could only change 1 or 2 extinctions at a time because the matrix was very ill conditioned. This made for very slow convergence and the devouring of much Cray CPU time. The nice thing about singular value

decomposition is that you can make it as stable as you want, so now I can do all the extinctions at once, with an overall reduction of about a factor of 10 in CPU time. (I'm sure that, per iteration, SVD is slower than normal matrix inversion. I couldn't say by how much because, in my problem, it takes much more time to set up the matrix in the first place than it does to do either one.)

... and a caveat

This experience has highlighted one thing about SVD which is not made clear in Numerical Recipes — you need to be a little careful about how you define the cutoff level for the singular values. Numerical Recipes suggests (rather strongly) that you ignore any singular values for which $s_m/s_m(\text{max})$ is less than the fractional error in your data, and this is fine if all your free parameters are about the same size. In my problem, however, the free parameters (the atmospheric extinctions) vary from $\sim 10^{-6}$ at the outer limit of the detectable atmosphere to $\sim 10^{-2}$ at the deepest level visible — a range of four orders of magnitude. So if all the free parameters change by about the same fractional amount (a reasonable expectation in this case) singular vectors dominated by terms at the outer edge of the atmosphere will “naturally” have associated singular values 10,000 times as large as singular vectors dominated by terms from the deepest layers. I am claiming (hopeless optimist that I am) a fractional accuracy of 0.001 in my data. So if I slavishly followed Numerical Recipes, the extinctions in the deepest layers would never change because the SVD algorithm would consider them ill-constrained, when in fact they are well defined by the data.

In this case, since I know that a “reasonable” variation in any given extinction is proportional to the extinction itself, I just divide all the derivatives by their corresponding extinctions to give $d(\ln \text{extinction})$, which should be about the same everywhere, and do the SVD on those.

A Graphic Example

(Rated **R** — no children under 17 admitted
without parent or guardian)

Let us consider the following set of data points:

x	y
-0.4	-0.3
-0.3	-0.2
-0.2	-0.1
-0.1	0.0
0.0	0.1
0.1	0.2
0.2	0.3
0.3	0.4
0.4	0.5

Now, any fool can plainly see that these points are fit exactly by the function $y=x+0.1$. However, since none of us are fools, we miss this observation and decide instead to fit these points to the function $y=d+c \tanh(ax+b)$. (This undoubtedly qualifies us as imbeciles, but at least we're not fools.) So, after assigning initial values of $a=0$, $b=0$, $c=1$, and $d=0$, we're off, using the standard normal equation matrix inversion algorithm, and the **Imsl** program **Dlinrg** to invert the double-precision general matrix. And the result of our first iteration is:

Current value of free parameters				χ^2 per degree of freedom
↓	↓	↓	↓	↓
a	b	c	d	ssq = 13.80
0.000	0.000	1.000	0.000	

```

*** FATAL   ERROR 2 from DLINRG. The input matrix is singular. Some of
***         the diagonal elements of the upper triangular matrix U of the
***         LU factorization are close to zero.
    
```

Oops. Now we get to figure out for ourselves why the coefficient matrix is singular, and how to fix it. There is a way in **Imsl** to keep the program from stopping at this point, but the matrix would still be singular and anything returned for the inverse would still be garbage.

Starting over.

a	b	c	d	ssq = 1.819
1.000	0.000	1.000	0.000	
da ,	db ,	dc ,	dd	=
20.12,	-5.0E-15,	-18.65,	4.64E-15	* 1.957 used
-8.6E-15,	0.4010,	7.94E-15,	-0.3762	* 84.44 used
-18.65,	4.62E-15,	17.31,	-4.3E-15	* 2.140 used
8.00E-15,	-0.3762,	-7.4E-15,	0.3540	* 90.00 used

\uparrow
 $(C^{-1})^T$

\uparrow
 \vec{F}

(from Eq. 7)

All the numbers that go into the calculation of the Δp 's are shown. The change in any of the four free parameters is found by multiplying the four numbers in the column below d'p' by the corresponding numbers after the '*'s, and adding the results.

For example $\Delta a = 20.12 * 1.957 - 8.6e-15 * 84.44 - 18.65 * 2.14 + 8e-15 * 90$.

The mysterious notation 'used' is included for comparison with the SVD procedure, where it will actually mean something.

Now we iterate:

a	b	c	d		ssq = 1.075
0.4587	6.993E-8	1.540	0.1000		
da	db	dc	dd	=	
158.3,	-2.31E-5,	-523.1,	7.222E-5	* 26.98	used
-2.31E-5,	3.236,	7.708E-5,	-4.916	* -5.72E-5	used
-523.1,	7.708E-5,	1728.,	-2.40E-4	* 8.169	used
7.222E-5,	-4.916,	-2.40E-4,	7.468	* -3.66E-5	used

a	b	c	d		ssq = 4.006
0.1285	2.176E-7	3.289	0.1000		
da	db	dc	dd	=	
5380.,	-9.08E-3,	-137600.,	0.05982	* 113.8	used
-9.08E-3,	110.6,	0.2324,	-363.4	* -7.80E-4	used
-137600.,	0.2324,	3.518E6,	-1.530	* 4.450	used
0.05982,	-363.4,	-1.530,	1194.	* -2.36E-4	used

a	b	c	d		ssq = 19.59
-0.02377	1.120E-6	11.68	0.09999		
da	db	dc	dd	=	
362300.,	17.07,	1.780E8,	-398.9	* 895.5	used
17.07,	7452.,	8390.,	-87050.	* -0.07966	used
1.780E8,	8390.,	8.749E10,	-196000.	* -1.822	used
-398.9,	-87050.,	-196000.,	1.017E6	* -6.82E-3	used

a	b	c	d		ssq = 122.8
-0.06655	1.267E-5	-63.09	0.09994		
da	db	dc	dd	=	
202.3,	0.03847,	-191700.,	4.856	* 12100.	used
0.03847,	4.161,	-36.46,	262.4	* -48.99	used
-191700.,	-36.46,	1.817E8,	-4602.	* 12.77	used
4.856,	262.4,	-4602.,	16550.	* 0.7770	used

Doesn't seem to be converging very well. Look at the bounce c just took.

a	b	c	d		ssq = 1.239
-0.05863	1.093E-5	-22.54	0.1002		
da	db	dc	dd	=	
2632.,	0.4905,	-1.011E6,	22.11	* 434.4	used
0.4905,	54.13,	-188.5,	1220.	* -1.425	used
-1.011E6,	-188.5,	3.888E8,	-8501.	* 1.130	used
22.11,	1220.,	-8501.,	27490.	* 0.06326	used

a	b	c	d	ssq = 0.05492
-0.03644	5.983E-6	-25.59	0.1002	
da ,	db ,	dc ,	dd =	
13680.,	2.245,	-9.602E6,	114.9	* -103.8 used
2.245,	281.3,	-1576.,	7198.	* 0.3477 used
-9.602E6,	-1576.,	6.741E9,	-80650.	* -0.1479 used
114.9,	7198.,	-80650.,	184100.	* -0.01359 used

a	b	c	d	ssq = 1.111
-0.01690	9.219E-7	-41.16	0.1001	

```

*** WARNING ERROR 1 from DLINRG. The matrix is too ill-conditioned. An
*** estimate of the reciprocal of its L1 condition number is RCOND
*** = 9.453427705457240D-19. The inverse might not be accurate.

```

da ,	db ,	dc ,	dd =	
114200.,	6.229,	-2.781E8,	512.8	* -751.6 used
6.229,	2.49.,	-15170.,	96680.	* 2.920 used
-2.781E8,	-15170.,	6.773E11,	-1.249E6	* -0.3086 used
512.8,	96680.,	-1.249E6,	3.980E6	* -0.07094 used

Well, the coefficient matrix has been getting more and more ill-conditioned, and now it's bad enough for **Imsl** to start complaining about it. Notice how we are now summing four terms of order 10^6 to get a result of order 1? This is not good, and it's only going to get worse.

a	b	c	d	ssq = 4.000
-4.76E-3	-5.09E-6	-88.73	0.09983	

```

*** WARNING ERROR 1 from DLINRG. The matrix is too ill-conditioned. An
*** estimate of the reciprocal of its L1 condition number is RCOND
*** = 1.033296104432083D-22. The inverse might not be accurate.

```

da ,	db ,	dc ,	dd =	
3.893E6,	-4162.,	-7.25E10,	-738400.	* -3074. used
-4160.,	80090.,	7.748E7,	7.107E6	* 22.84 used
-7.25E10,	7.752E7,	1.351E15,	1.375E10	* -0.1650 used
-738200.,	7.107E6,	1.375E10,	6.306E8	* -0.2574 used

a	b	c	d	ssq = 18.89
8.107E-4	-3.03E-5	-313.8	0.09617	

```

*** WARNING ERROR 1 from DLINRG. The matrix is too ill-conditioned. An
*** estimate of the reciprocal of its L1 condition number is RCOND
*** = 2.221655737398928D-28. The inverse might not be accurate.

```

da ,	db ,	dc ,	dd =	
3.381E8,	1.172E7,	1.309E14,	7.637E9	* -23610. used
1.245E7,	8.117E6,	4.819E12,	2.692E9	* 1599. used
1.309E14,	4.536E12,	5.064E19,	2.955E15	* 0.06117 used
7.866E9,	2.684E9,	3.044E15,	9.342E11	* -5.097 used

```

      a      b      c      d      ssq = 144.4
1.705E-3  -4.37E-4  1591.  0.01621

```

```

*** WARNING ERROR 1 from DLINRG. The matrix is too ill-conditioned. An
*** estimate of the reciprocal of its L1 condition number is RCOND
*** = 6.782663154674431D-28. The inverse might not be accurate.

```

```

      da ,      db ,      dc ,      dd      =
742600., 190700., -6.93E11, -6.061E8 * -163600. used
190600., 64140., -1.78E11, -1.797E8 * 1.115E6 used
-6.93E11, -1.78E11, 6.466E17, 5.656E14 * -0.4814 used
-6.059E8, -1.798E8, 5.654E14, 5.330E11 * 700.9 used

```

c just bounced again, even further than last time.

```

      a      b      c      d      ssq = 1.367
1.408E-3  -3.39E-4  855.2  0.3209

```

```

*** WARNING ERROR 1 from DLINRG. The matrix is too ill-conditioned. An
*** estimate of the reciprocal of its L1 condition number is RCOND
*** = 7.101782323777782D-28. The inverse might not be accurate.

```

```

      da ,      db ,      dc ,      dd      =
5.789E6, 1.406E6, -3.52E12, -2.397E9 * -10470. used
1.406E6, 455000., -8.54E11, -6.791E8 * 53450. used
-3.52E12, -8.54E11, 2.136E18, 1.456E15 * -0.03844 used
-2.396E9, -6.791E8, 1.456E15, 1.075E12 * 62.50 used

```

etc., etc., for 20 iterations...

```

      a      b      c      d      ssq = 4.988E-3
5.265E-4  1.211E-4  1861.  -0.1244

```

```

*** WARNING ERROR 1 from DLINRG. The matrix is too ill-conditioned. An
*** estimate of the reciprocal of its L1 condition number is RCOND
*** = 3.611280490358226D-31. The inverse might not be accurate.

```

```

      da ,      db ,      dc ,      dd      =
7.104E7, -1.721E7, -2.51E14, 6.246E10 * 2230. used
-1.736E7, 5.474E6, 6.135E13, -1.76E10 * -1776. used
-2.51E14, 6.085E13, 8.877E20, -2.21E17 * 5.153E-4 used
6.272E10, -1.76E10, -2.22E17, 5.954E13 * -0.9543 used

```

```

      a      b      c      d      ssq = 1.745E-3
4.836E-4  1.300E-4  2045.  -0.1645

```

```

*** WARNING ERROR 1 from DLINRG. The matrix is too ill-conditioned. An
*** estimate of the reciprocal of its L1 condition number is RCOND
*** = 1.195482375519446D-31. The inverse might not be accurate.

```

```

      da ,      db ,      dc ,      dd      =
1.242E8, -3.502E7, -5.25E14, 1.399E11 * 1333. used
-3.328E7, 1.091E7, 1.407E14, -4.06E10 * -2491. used
-5.25E14, 1.481E14, 2.221E21, -5.92E17 * 1.568E-4 used
1.363E11, -4.16E10, -5.76E17, 1.599E14 * -1.218 used

```

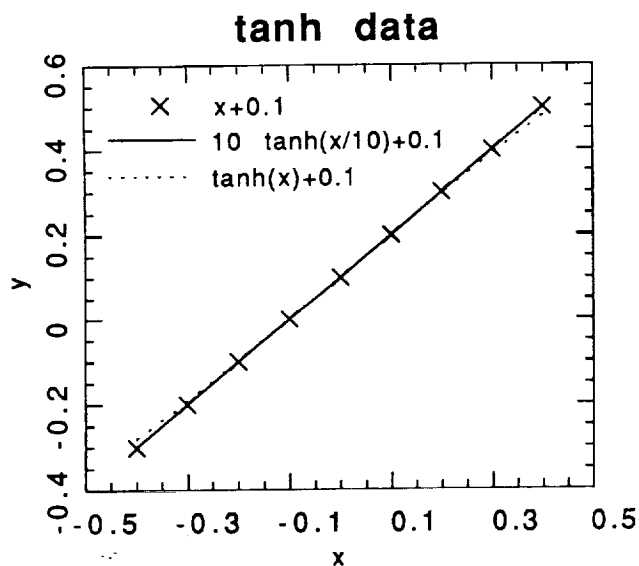
x	y	y_c
-0.4	-0.3	-0.2943
-0.3	-0.2	-0.1954
-0.2	-0.1	-0.0965
-0.1	0.0	0.0024
0.0	0.1	0.1014
0.1	0.2	0.2003
0.2	0.3	0.2992
0.3	0.4	0.3981
0.4	0.5	0.4970

final calculated values of y

Actually, it's rather remarkable how well we've gotten away with adding terms of order 10^{13} to get a result accurate to order 10^{-4} for a and b . But the nasty fact is that this algorithm, and the value of c in particular, is never going to converge. You can show analytically that the mathematical best fit of a tanh function to this particular data set is

$$y = \lim_{\epsilon \rightarrow 0} 0.1 + \tanh(\epsilon x)/\epsilon$$

and it doesn't matter whether ϵ is positive or negative.



In practice, once ϵ gets small enough, changing it further results in insignificant changes in χ^2 . Do you have any problem with the $\epsilon=0.1$ fit? I don't.

Now let's try singular value decomposition.

x	y
-0.4	-0.3
-0.3	-0.2
-0.2	-0.1
-0.1	0.0
0.0	0.1
0.1	0.2
0.2	0.3
0.3	0.4
0.4	0.5

same data set

Fit to $y=d+c \tanh(ax+b)$.

Start with $a=0$, $b=0$, $c=1$, $d=0$,
just like last time...

	a	b	c	d	ssq = 13.80		
s	0.000	0.000	1.000	0.000			
i v	da ,	db ,	dc ,	dd	=		
ne →	0.0000,	-0.7071,	0.0000,	-0.7071	* -3.000	/ 42.43	used
gc →	1.0000,	0.0000,	0.0000,	0.0000	* 7.746	/ 7.746	used
ut →	0.0000,	-0.7071,	0.0000,	0.7071	* 0.000	/ 2.62E-16	ignored
lo →	0.0000,	0.0000,	1.0000,	0.0000	* 0.000	/ 0.000	ignored
ar					↑	↑	
rs					↑	↑	
	V^T				$U^T_{(m)} \cdot \vec{B}$	s_m	(Eq. 10)

... and the matrix is singular, just like the last time. However, unlike last time, the program doesn't complain piteously and die. Inspection of the singular values and the associated singular vectors shows that c is totally unconstrained (because c and d are formally degenerate for $a=b=0$) and so is $b-d$. However, something useful is known about both a and $b+d$, so changes are made to bring these two quantities into line, while the other two singular vectors are ignored. (Note that now 'used' actually means something.)

Note: Don't get carried away over this. SVD can get around some singular conditions, but not all of them. For example, if we had started with all the free parameters set to zero, this algorithm would have set $d=0.1$ and quit, insisting that a , b , and c were unconstrained. (I'll bet you were wondering why I didn't do that, weren't you?)

a	b	c	d	ssq = 0.02430		
1.000	0.05000	1.000	0.05000			
da ,	db ,	dc ,	dd	=		
0.0051,	-0.6837,	-0.0332,	-0.7290	* -0.08986	/ 41.14	used
-0.6789,	0.0484,	-0.7324,	-0.0168	* -0.3017	/ 10.17	used
-0.0814,	-0.7275,	0.0116,	0.6811	* 0.08285	/ 1.150	used
0.7297,	-0.0313,	-0.6799,	0.0653	* -0.1247	/ 0.1623	used

Quite an improvement in ssq, isn't it?

a	b	c	d	ssq = 1.161		
0.4539	0.02167	1.545	0.05099			
da	db	dc	dd	=		
0.0017,	-0.8359,	-0.0115,	-0.5487	*	-0.4724 / 54.67	used
-0.9581,	0.0069,	-0.2862,	-0.0076	*	-2.362 / 12.19	used
-0.0217,	-0.5486,	0.0372,	0.8349	*	0.02498 / 0.2999	used
0.2856,	-0.0133,	-0.9574,	0.0413	*	-0.04009 / 0.02229	ignored

Well, I never said it was perfect.

a	b	c	d	ssq = 1.524E-3		
0.6378	-0.01814	1.603	0.1267			
da	db	dc	dd	=		
-0.0020,	-0.8421,	0.0092,	-0.5393	*	-0.04789 / 55.62	used
-0.9250,	-0.0074,	-0.3798,	0.0085	*	0.05002 / 12.80	used
0.0231,	-0.5392,	-0.0268,	0.8414	*	-0.01894 / 0.5911	used
0.3792,	0.0103,	-0.9246,	-0.0332	*	-0.04969 / 0.05919	used

But it is self-correcting.

a	b	c	d	ssq = 0.7804		
0.3151	-8.78E-3	2.379	0.1282			
da	db	dc	dd	=		
-0.0006,	-0.9209,	0.0034,	-0.3897	*	0.2197 / 76.98	used
-0.9912,	-0.0007,	-0.1323,	0.0020	*	-1.963 / 18.37	used
0.0044,	-0.3897,	-0.0170,	0.9208	*	-7.07E-3 / 0.1598	used
0.1323,	0.0036,	-0.9911,	-0.0174	*	-0.01865 / 7.766E-3	used

a	b	c	d	ssq = 3.132		
0.1031	-2.85E-3	4.774	0.1278			
da	db	dc	dd	=		
0.0001,	0.9787,	-0.0006,	0.2052	*	-0.4264 / 146.2	used
-0.9998,	0.0000,	-0.0216,	0.0001	*	-3.934 / 36.94	used
0.0002,	-0.2052,	-0.0057,	0.9787	*	-1.03E-3 / 0.01826	ignored
-0.0216,	-0.0006,	0.9998,	0.0057	*	2.697E-3 / 2.759E-4	ignored

In general, whenever the singular vector dominated by 'dc' is used, ssq goes up. But the singular value associated with this vector keeps going down, reflecting the fact that as c gets larger its influence on χ^2 decreases. So this singular vector gets ignored more and more often.

a	b	c	d	ssq = 1.229E-5		
0.2096	-5.70E-3	4.776	0.1272			
da	db	dc	dd	=		
-0.0003,	-0.9787,	0.0012,	-0.2055	*	1.010E-3 / 146.0	used
-0.9990,	0.0002,	-0.0440,	0.0005	*	-5.05E-3 / 36.84	used
0.0010,	-0.2055,	-0.0114,	0.9786	*	-2.10E-3 / 0.07532	used
-0.0440,	-0.0012,	0.9990,	0.0114	*	5.525E-3 / 2.310E-3	ignored

a	b	c	d	ssq = 6.118E-6		
0.2097	9.784E-6	4.777	0.09996			
da	db	dc	dd	=		
0.0000,	-0.9787,	0.0000,	-0.2055	*	7.013E-5 / 146.0	used
0.9990,	0.0000,	0.0440,	0.0000	*	2.510E-4 / 36.84	used
0.0000,	-0.2055,	0.0000,	0.9787	*	3.309E-6 / 0.07539	used
0.0440,	0.0000,	-0.9990,	0.0000	*	-5.52E-3 / 2.314E-3	used

a	b	c	d	ssq = 0.7552	
0.1047	5.172E-6	7.161	0.09995		
da	db	dc	dd	=	
0.0000,	-0.9904,	0.0000,	-0.1384	* -3.30E-4 / 216.8	used
0.9999,	0.0000,	0.0146,	0.0000	* 1.943 / 55.41	used
0.0000,	-0.1384,	0.0000,	0.9904	* 1.285E-6 / 0.01903	ignored
0.0146,	0.0000,	-0.9999,	0.0000	* -2.07E-3 / 2.883E-4	ignored

a	b	c	d	ssq = 1.332E-6	
0.1397	6.684E-6	7.162	0.09995		
da	db	dc	dd	=	
0.0000,	-0.9904,	0.0000,	-0.1385	* -2.51E-7 / 216.7	used
0.9998,	0.0000,	0.0195,	0.0000	* 7.938E-4 / 55.36	used
0.0000,	-0.1385,	0.0000,	0.9904	* 1.527E-6 / 0.03390	used
0.0195,	0.0000,	-0.9998,	0.0000	* -2.46E-3 / 6.858E-4	ignored

a	b	c	d	ssq = 1.206E-6	
0.1397	4.481E-7	7.162	0.1000		
da	db	dc	dd	=	
0.0000,	-0.9904,	0.0000,	-0.1385	* 3.04E-10 / 216.7	used
0.9998,	0.0000,	0.0195,	0.0000	* -2.2E-11 / 55.36	used
0.0000,	-0.1385,	0.0000,	0.9904	* -6.3E-10 / 0.03391	used
0.0195,	0.0000,	-0.9998,	0.0000	* -2.46E-3 / 6.860E-4	ignored

Habemus convergence! And after only 11 iterations (including the one used to escape from the singularity). Note the final value of c : 7 instead of 2000. And the final value of ssq : 10^{-6} instead of 10^{-3} . While the normal equation matrix inversion went off in obsessive pursuit of (unobtainable) perfection, SVD concentrated on getting the right values for the parameters that had the major influence on χ^2 .

x	y	y_c	
-0.4	-0.3	-0.29989	
-0.3	-0.2	-0.20005	
-0.2	-0.1	-0.10010	
-0.1	0.0	-0.00007	
0.0	0.1	0.10000	final calculated values of y
0.1	0.2	0.20007	
0.2	0.3	0.30010	
0.3	0.4	0.40005	
0.4	0.5	0.49989	

References

PRESS, W.H., B.P. FLANNERY, S.A. TEUKOLSKY, AND W.T. VETTERLING 1989. *Numerical Recipes (Fortran version)*. Cambridge University Press.

Appendix B

VOYAGER IMAGING OF TRITON'S CLOUDS AND HAZES

Kathy Rages

Space Physics Research Institute

Sunnyvale, California 94087

(415) 604-6735

Internet Address: rages@gal.arc.nasa.gov

James B. Pollack

Space Science Division

NASA Ames Research Center

Moffett Field, California 94035

(415) 604-5530

Thursday, June 25, 1992

30 Pages

5 Tables

6 Figures

Proposed running head: Triton Clouds and Hazes

Please direct editorial correspondence to:

Kathy Rages

Mail Stop 245-3

NASA Ames Research Center

Moffett Field, California 94035-1000

(415) 604-6735

Internet Address: rages@gal.arc.nasa.gov

SPAN Address: gal::rages

Abstract

Voyager images of Triton indicate considerable spatial variability in the concentration of at least two different scattering components in the atmosphere. Data from high phase angle limb scans have been fit to Mie scattering models to derive mean particle sizes, number densities, and vertical extent for both types of scattering material at ten different locations between 15°S and 70°S . These fits reveal an optically thin haze at latitudes between 10°S and $25\text{-}30^{\circ}\text{S}$. The imaging data can be fit reasonably well by both conservatively scattering and absorbing hazes with particle sizes near $0.17\text{ }\mu\text{m}$ and optical depths of order $0.001\text{-}0.01$. Rayleigh scattering haze fits the imaging data somewhat less well, and cannot simultaneously reproduce the imaging and UVS measurements. At high southern latitudes, Triton displays clouds below an altitude of $\sim 8\text{ km}$, as well as the haze at higher altitudes. The clouds have particle sizes which may range from $0.7\text{-}2.0\text{ }\mu\text{m}$, or may be near $0.25\text{ }\mu\text{m}$. The atmospheric optical depth poleward of 30°S must be generally greater than 0.1 , but need not be more than 0.3 . Horizontal inhomogeneities are quite noticeable, especially at longitudes east of (i.e. higher than) 180° .

1. Introduction

Until the Voyager encounter with Neptune very little was known about its largest satellite Triton. Even estimates of Triton's radius were uncertain. It was known from measurements of the infrared spectrum (Cruikshank *et al.* 1984, Cruikshank *et al.* 1989) that both methane ice and some form of condensed nitrogen were present on the surface, but the surface pressure and temperature and the atmospheric optical depth were unknown. From radio occultation and Ultraviolet Spectrometer data taken during the Voyager encounter (Tyler *et al.* 1989, Broadfoot *et al.* 1989, Gurrola *et al.* 1992) it was determined that Triton possessed an atmosphere which was mostly nitrogen, with a surface pressure of about $14 \mu\text{bar}$ and a surface temperature of 38K. Despite this exceedingly low pressure, images of Triton's limb taken near closest approach clearly show some kind of scattering layer above the surface (Smith *et al.* 1989). A detailed analysis of these images (Pollack *et al.* 1990) indicated that a thin haze, presumably of photochemical origin, is present nearly everywhere on Triton. In addition, a sizable fraction of the surface poleward of 30°S is covered by discrete clouds which are confined to the lower 8 km of the atmosphere and may have optical depths of order 0.1. The confinement of these clouds to the lower part of Triton's atmosphere and high southern latitudes suggests that they are composed of nitrogen ice.

In this paper, we will present the results of a detailed analysis of the Voyager images of Triton taken at the highest solar phase angles. Although the spatial resolution of these images is lower than that of the images studied in Pollack *et al.* (1990), observations at high phase angles are more sensitive to atmospheric properties such as the particle sizes of the hazes and clouds, and less influenced by scattering from the solid surface, than the highest resolution images were. In the next section, we outline our data analysis procedure. In sections 3 and 4 we discuss the properties of atmospheric models derived for low and high southern latitudes, respectively. Section 5 contains a more detailed discussion of localized atmospheric features, and the final section considers some implications of our findings for the haze and cloud pro-

duction mechanisms, and for Triton's thermal balance and for models of seasonal volatile transport.

2. Data analysis procedure

The data set we will be discussing in this paper consists of fifteen Voyager wide angle images of Triton taken at high solar phase angles (140° – 160°). Three of these images were taken with the violet filter, five with the blue filter, five with the green filter, and two with the orange filter. The linear resolution in these images ranged from about 10 kilometers per line pair (km/lp) at the beginning of the sequence (highest phase angle) to about 25 km/lp at the end of the sequence (lowest phase angle). Details of the images used are given in Table I. The phase angles given in Table I are for a point at the center of Triton's disk.

Initial processing of these images was the same as that outlined in Pollack *et al.* (1987), and included removal of blemishes and reseaux, dark current subtraction, and conversion (via a non-linear response function specific to each pixel) from DN value (0-255) to specific intensity (I/F) at each pixel. The precise pointing of each image was initially determined by fitting Triton's observed limb in the image to a circle of radius 1350 km, using the NAV program in the VICAR image handling package. Later the pointing was improved by comparing specific intensity profiles calculated from the best fitting atmospheric models to the observed I/F scans and determining whether all the I/F scans for a given image could be better fit by shifting the observed limb. This procedure converged (to within 0.1 pixels) after only one iteration.

After the initial processing of each image, specific intensity was measured as a function of tangent point radius at intervals of approximately one pixel along selected radial lines crossing the limb of each image, with averaging over ~ 10 pixels along the limb. The scan lines selected for all the images are shown projected onto the surface of Triton in Fig. 1. As can be seen in this figure, the scan lines were chosen to correspond to ten distinct areas along the limb. The numerical analysis described in the following sections was carried out by using all

the scans comprising a particular region to form a single data set covering a range of solar phase angles and wavelengths.

Before fitting the limb scans to the atmospheric models a final background subtraction was carried out by fitting a quadratic function in radius to the portions of each limb scan well above the limb and well inside the terminator. This is necessary at high phase angles because some sunlight is scattered from the sunshade into the camera, and this is not included in the standard dark current subtraction. Also, the dark current is proportional to the camera temperature, and it is generally not possible to find a dark current frame taken at the same temperature as a given image.

The spatial resolution of the high phase angle Triton images was not high enough to obtain meaningful vertical extinction profiles by directly inverting the radial intensity profiles. Instead, the radial intensity profiles were fit to simple exponential models of the extinction as a function of altitude.

For a given atmospheric model, I/F as a function of tangent point radius was calculated for an atmosphere consisting of concentric homogeneous spherical shells using methods described in Rages and Pollack (1983) and Pollack *et al.* (1987). Briefly, for each line of sight the incoming (from the sun) and outgoing (toward the Voyager camera) atmospheric optical depths are assumed to vary linearly between the spherical shell boundaries. The specific intensity due to singly scattered light can then be calculated as the sum of the analytic functions describing I/F due to scattering from each shell. Multiply scattered light is treated in an empirical fashion which converges to the equivalent plane parallel case for lines of sight well inside the limb (and away from the terminator). High solar phase angles are favored for this treatment because multiple scattering tends to be relatively unimportant for such scattering geometries.

Specific intensities were calculated in this way at 30-50 points along each radial scan at ten wavelengths between $0.3 \mu\text{m}$ and $0.65 \mu\text{m}$, then convolved over both the various filter re-

sponse functions (Danielson *et al.* 1981) and the point spread function (S.A. Collins, private communication) of the Voyager camera.

3. Low latitudes (haze only)

At latitudes near the equator the atmospheric model contained a single component (haze), with a number density varying exponentially with altitude. The single scattering properties of the haze were described by Mie theory, with a complex refractive index and particle size that did not vary with altitude. The real part of the haze refractive index was assumed to be 1.44, consistent with the value for ethane ice. The particle sizes were distributed according to a fairly narrow (width parameter 0.05) Hansen-Hovenier size distribution (Hansen and Hovenier 1974) with a cross section weighted mean radius r_h .

It was assumed that there were no horizontal variations in the atmospheric properties over the entire area covered by the limb scans in any one region. This is a reasonably good assumption at low latitudes, but some of the higher latitude regions cover more than 30° of latitude, and in some cases (discussed in more detail in section 5) this assumption is clearly violated.

At high phase angles the surface generally contributes relatively little to the total observed I/F. The surface locations seen at high phase angles were also mostly hidden in the high spatial resolution images taken at intermediate phase angles, so local variations in the surface photometry are not well defined. Therefore, Triton's surface photometric properties were described by a single Hapke photometric function for each filter, with parameters given by Hillier *et al.* (1991) for the violet, blue, and green filters. Orange filter parameters were estimated by extrapolating from blue and green.

The low latitude data were fit using three different types of scattering haze, as outlined in Table II. The first was composed of particles in which the imaginary part of the refractive index was assumed to be a linear function of wavelength, $m_{ih} = a_h + b_h \lambda$ (case *a1*). The

second was composed of Mie scatterers with $m_{ih} = 0$ (case *b1*). The third was composed of very small nonabsorbing particles for which the phase function was effectively that of Rayleigh scatterers (case *c1*).

The haze column number density n_h , scale height H_h , mean particle radius r_h (in cases *a1* and *b1*), and a_h and b_h (in case *a1*) were treated as free parameters in a least squares fitting procedure.

Results are shown in Fig. 2 for a region near 15°S, 275°E (region 10). Haze models of Fig. 2 all three types were found which gave acceptable fits to the imaging data: particles with a mean radius of 0.17 μm and an imaginary index of 0.05 (case *a1*), conservatively scattering particles with 0.17 μm radius (case *b1*), and Rayleigh scattering (case *c1*). The details of these three cases can be found in Table III, together with the weighted sum of the squared residuals χ^2 Table III divided by the number of degrees of freedom in each data set. The error bars given in Table III are formal 1σ confidence levels from the least squares fit and do not include the effects of any possible systematic errors.

Since the derived particle sizes are small enough for the phase function to be diffraction dominated at the scattering angles corresponding to the Voyager observations, these results should change very little if the haze is taken to be condensed acetylene (refractive index 1.33) or ethylene (1.36) instead of ethane ice. The variation of the imaginary index with wavelength was not well determined, and even the constant portion is not significantly different from zero, as indicated by the error bars in case *a1* and the fact that χ^2 is the same for both case *a1* and case *b1*. The (radial) extinction optical depths to the surface for these models generally lie between 0.001 and 0.01 in all four filters, as shown in Table IV.

Table IV

The Rayleigh scattering case fits the imaging data somewhat less well than the other two, and can be eliminated entirely by a comparison with data from the Voyager Ultraviolet Spectrometer (see Krasnopolsky *et al.* 1992). The Rayleigh scattering case predicts ultraviolet (slant) optical depths to the surface of around 10, which is an order of magnitude larger than

those seen by the UVS. There is a pointing uncertainty of ~5 km in the UVS data (F. Herbert, private communication), which might mean that their slant optical depths refer not to the surface, but to the altitude at which an optically thick (in the UV) scattering layer is encountered. Even at 5 km altitude, the Rayleigh scattering case predicts a slant optical depth in the UV of 6, assuming that the haze is conservatively scattering at the wavelengths seen by the UVS. In fact, many photochemically produced hydrocarbons have absorption edges between 0.3 μm and 0.165 μm (the long wavelength limit of the UVS data). The addition of any UV absorption would only serve to increase the predicted optical depth.

The other two cases predict UV optical depths of about 0.15 if the imaginary index in the UV is given by extrapolating the function used between 0.3 μm and 0.65 μm , and UV absorption not adequately modelled by this simple linear function could raise the UV optical depth of either model to the 0.5-1.0 range observed.

The data from regions 1 and 9 were also fit to single component scattering models of type *a1*, and the details of these cases are also given in Table III. In both cases the derived imaginary index is very steeply sloping (in one case rising and in the other falling toward the red).

4. High latitudes (haze + cloud)

In light of the findings of Pollack *et al.* (1990) that both the haze and optically thicker discrete clouds can be present south of about 30°S, at these latitudes several two component models were fit to the data. These models contained the 0.17 μm conservatively scattering haze above an altitude of 8 km, with the column number density n_h and scale height H_h left as free parameters. Below 8 km there was another scattering component (cloud), with an independent exponential altitude profile defined by n_c and H_c , a particle radius r_c , and imaginary part of the refractive index defined as a linear function of wavelength $m_{ic} = a_c + b_c \lambda$.

The spatial distribution of the discrete cloud particles provides good evidence for their being produced by the condensation of nitrogen vapor, as outlined in Pollack *et al.* (1990). In particular, they exhibit sizeable variations in brightness on length scales of hundreds of kilometers, they preferentially occur at latitudes poleward of 30 degrees south, and they are confined to the bottom 8 kilometers of the atmosphere. The brightness variations may reflect some combination of local variations in optical depth or surface albedo and the presence or absence of surface nitrogen ice at the time of the Voyager flyby; preference for high southern latitudes may be related to the subsolar point being located near 45°S latitude at the time of the Voyager flyby; and the confinement in altitude may be related to the static stability profile of the atmosphere (Yelle *et al.* 1991). It is highly unlikely that the cloud particles are composed primarily of methane ice rather than nitrogen ice since the mixing ratio of methane in Triton's lower atmosphere is more than four orders of magnitude smaller than that of nitrogen, and since both materials are in vapor pressure equilibrium with surface deposits of their corresponding ices. Carbon monoxide has a mixing ratio of a few percent at most (Broadfoot *et al.* 1989) in the troposphere, so it should not make any major contribution to a condensation cloud, either. Therefore, the real part of the cloud refractive index was taken to be 1.25, consistent with measured values for nitrogen ice (Thompson *et al.* 1973).

Two-component models were applied to all the regions shown in Fig. 1 except region 10. It soon became clear that large cloud optical depths (~ 1) were favored by the fitting algorithm. Optical depths this large are excluded by the images taken at lower phase angles and higher spatial resolutions, which show little or no indication of surface obscuration. We have no way of calculating directly the surface contrast predicted for these images by a given model atmosphere, since all the radiative transfer codes we have access to (including plane parallel adding-doubling codes) assume horizontal homogeneity. As a substitute, we have estimated the maximum optical depth consistent with the surface detail seen at intermediate phase angles and included that as an additional constraint on the models used to fit the high phase angle

observations, specifying an upper bound τ_l on the total atmospheric optical depth. The function to be minimized by the least squares fitting procedure was then

$$\chi^2 = \sum_{j=1}^N \frac{(I/F_c - I/F_o)_j^2}{\sigma_{oj}^2} + \sum_{i=V,B,G,O} f(\tau_i)^2 \quad (1)$$

where the first summation is the usual formulation of χ^2 as the weighted sum over all N data points of the squares of the differences between the calculated and observed values of the dependent variable (in this case specific intensity), and the second term is the sum over all the filters of

$$\begin{aligned} f(\tau_i) &= 0 & \tau_i < \tau_l \\ f(\tau_i) &= \frac{(\tau_i - \tau_l)}{\sigma_\tau} & \tau_i > \tau_l \end{aligned} \quad (2)$$

where σ_τ controls the "hardness" of the upper bound. Initially τ_l was set to 0.3 and σ_τ was set to 0.05.

Without the optical depth constraint, χ^2 declines only slowly with increasing optical depth above $\tau = 0.3$ (which already corresponds to a slant optical depth of ~ 6 at Triton's limb), and the difference between $\chi^2(0.3)$ and $\chi^2(\infty)$ is not statistically significant. This slight preference for large optical depths may stem from the fact that there is no way to alter the scattering behavior of the solid surface within the context of our models, or it may be due to small changes in the shape of the calculated radial intensity profiles caused by our approximate treatment of multiple scattering in the atmosphere (Pollack *et al.* 1987).

Three variations on the two component model were fitted to the high latitude data. The first contained fairly large cloud particles ($r_c > 0.6 \mu\text{m}$) and an optical depth constrained at $\tau = 0.3$ (case *a2*). The second (case *b2*) also had an optical depth constrained at $\tau = 0.3$, but was characterized by cloud particles not much larger than the photochemical haze above them

($r_c < 0.3 \mu\text{m}$). The third (case $c2$) contained the smaller cloud particles and had an optical depth constrained at $\tau = 0.1$ ($\tau_l = 0.08$ and $\sigma_\tau = 0.02$). These three cases are summarized in Table II.

Results for a typical high latitude region (region 3, near 50°S , 124°E) are shown in Fig. 3, and the corresponding values of the various free parameters, with formal 1σ confidence levels, are given in Table V. Cases $a2$ and $b2$ fit the data for this region almost equally well. Case $a2$ contains cloud particles with a mean radius of $1.5 \mu\text{m}$ (solid line), while for case $b2$ this quantity is $0.22 \mu\text{m}$ (dashed line). Figure 4 illustrates how these two very different particle sizes could both fit the observations. It shows the albedo-weighted single scattering phase function for both cases and all four filters. Although the larger particles have a much larger diffraction peak than the smaller particles, it is confined to scattering angles less than 20° (phase angles $>160^\circ$), outside the range of the Voyager observations. (The scattering angle of each image in the data set is shown by a vertical line.) Between 20° and 40° scattering angle, the range which is covered by the observations, the two sets of phase functions are very similar. Diffraction is the dominant contributor to the phase function of the smaller particles at these scattering angles, while the dominant term for the larger particles is light which is transmitted through a particle without reflection, but with refraction at each encounter with the particle surface.

Fig. 3

Table V

Fig. 4

The effect of lowering the atmospheric optical depth on the fit to the data was found by changing τ_l and σ_τ to 0.08 and 0.02 respectively, which limited the optical depth to around 0.1 (case $c2$). The result is shown in Table V and as the dotted line in Fig. 3. Forcing the optical depth to be this low in this region increases χ^2 by a factor of 5.

The optimum cloud scale height is more than 16 km, making the total thickness of the cloud layer (8 km) less than half a scale height. It was not possible to determine from the high phase angle data alone whether the cloud was uniformly mixed with the gas, which has a scale height of around 16 km (Gurrola *et al.* 1992), or whether the cloud mixing ratio increased with

altitude as might be the case if condensation were occurring at the top of the cloud layer. However, Pollack *et al.* (1990) found a strong increase in cloud brightness towards the base of the atmosphere in the highest resolution images of Triton's limb, which strongly implies that uniform mixing is more probable.

The best fitting values of a_c and b_c yield $m_{ic} \sim 0.0-0.013$ (for $1.5 \mu\text{m}$ particles) or $m_{ic} \sim 0.1-0.03$ (for $0.22 \mu\text{m}$ particles) for wavelengths from $0.3 \mu\text{m}$ to $0.65 \mu\text{m}$. Cloud particles which are conservatively scattering at all wavelengths do not fit the variation in the peak I/F with wavelength and phase angle. Nitrogen ice does not absorb at these wavelengths, so the cloud absorption is probably due to some admixture of complex hydrocarbons derived from the diffuse haze. This could indicate that the diffuse haze is not conservatively scattering either.

The best fitting parameter values for each two-component model studied for all of the regions 1-9 are given in Table V. The total (vertical) optical depths for all the models (both one- and two-component) are given in Table IV. Most of the high latitude regions were similar to region 3 in having both cases $a2$ and $b2$ fit the data almost equally well. At the highest latitudes (regions 5, 6, and 7) r_c was near either $0.7 \mu\text{m}$ or $0.3 \mu\text{m}$. Region 9 was greatly affected by horizontal inhomogeneities in the atmospheric scatterers (see next section). Haze column number densities at high latitudes are about the same as they are at low latitudes (although at high latitudes the haze optical depth is given for 8 km altitude, while at low latitudes it is given at the surface). In the two regions for which both one- and two-component models were tried (regions 1 and 9) the two-component models give significantly better fits to the observations.

5. Horizontal inhomogeneities

Many regions (especially those east of 180° longitude) showed features in the radial intensity profiles that can only be due to local variation in the atmospheric scattering properties.

Figure 5 shows the complete data set from region 6, near 70°S , 175°E . In this region, most Fig. 5

of the limb scans show a pronounced hump on the portion of the curve inside Triton's limb (radius less than 1350 km), represented by open circles in Fig. 5. The surface is not bright enough in the scattering geometries represented by these scans for these humps to be due to variations in the surface properties, and this behavior cannot be produced by any extinction profile composed of homogeneous spherical shells. The most likely cause of the humps in this data set is a local increase in the cloud optical depth over part of the area covered by region 6. This is a strong indication that the "background" cloud optical depth in this region must be considerably less than unity.

The data points shown as open circles in Fig. 5, and similar data points in the other regions, were not included in the data set used to define the values of the free parameters given in Table V, because the two-component atmospheric model itself is inadequate for reproducing them. The locations of all such data points are shown in Fig. 6.

Fig. 6.

The most pronounced local variations in Triton's atmospheric scatterers seem to be concentrated in a diagonal band between 55° and 15° south latitude, and 180° and 270° east longitude. A comparison of Fig. 6 with Fig. 1 shows that this apparent concentration is not merely a selection effect. The part of Triton covered by the high phase angle images is (more or less inevitably) outside the region covered at the highest spatial resolution at lower phase angles. Therefore the characteristics of the surface in the band of local atmospheric variability are known only vaguely. According to McEwen (1990), this band lies mostly over the bright south polar cap, with its northern end extending into the brighter polar cap fringe. The band of pronounced atmospheric variability lies along the evening terminator, so it could be an indicator of some kind of diurnal effect.

The plumes visible on the highest resolution images of Triton (Soderblom *et al.* 1990), marked by \times 's in Fig. 6, are also in the opposite hemisphere from the areas of local variability seen at high phase angles. One area which Pollack *et al.* (1990) noted as unusual because it

lacked the otherwise ubiquitous haze is somewhat closer to the variable regions (dashed ellipse in Fig. 6).

6. Discussion

We have found 0.001-0.01 optical depths of $\sim 0.17 \mu\text{m}$ particles vertically distributed with scale heights of ~ 10 km in Triton's atmosphere everywhere we have looked. In addition, tropospheric clouds with optical depths of a few tenths and particle sizes of either $0.2\text{-}0.3 \mu\text{m}$ or $0.6\text{-}1.7 \mu\text{m}$ are generally present south of $25^\circ\text{-}30^\circ\text{S}$. We will now consider some of the implications of these findings.

There are a number of properties of the haze particles that support the hypothesis that they are made of photochemically produced gases that condensed in the cold, lower atmosphere of Triton. These include the nearly ubiquitous presence of the haze particles at all locations covered by the limb images and their presence throughout at least the bottom several tens of kilometers of the atmosphere (Smith *et al.* 1989, Pollack *et al.* 1990); their mean size (comparable to that of haze particles in the atmospheres of Titan and the outer planets) (Krasnopolsky *et al.* 1992 and this paper); and their scale height and column mass density. These last two properties of the haze material support the proposed identification in the following manner.

The photochemistry of methane is initiated chiefly by Lyman α photons from the sun and the interstellar medium (Strobel *et al.* 1990). Given the methane profile measured by the Voyager UVS, optical depth unity for Lyman α absorption by methane occurs at altitudes of about 10 and 20 km in the summer and winter hemispheres, respectively. At the cold temperatures of Triton's lower atmosphere, the reaction products quickly condense into small ice particles, which then fall to the surface. According to the calculations of Strobel *et al.* (1990), C_2H_4 ice is the most abundant reaction product, with slightly smaller amounts of C_2H_2 and C_2H_6 ice and much smaller amounts of C_4H_2 ice also being generated.

According to section 3, the haze scale height in the southern hemisphere averages about 9 km. This is distinctly smaller than the nitrogen gas scale height (around 16 km) between 8 and 20 km altitude, but is very close to the CH_4 scale height at these altitudes. As demonstrated by Krasnopolsky *et al.* (1992), if the haze particles were generated entirely above 20 km, their scale height in the region below 20 km would equal the gas scale height: their sedimentation velocity is inversely proportional to the gas number density, their size would remain a constant below 20 km in this case, and therefore their number density and extinction and scattering coefficients would be directly proportional to the gas number density for steady state conditions (constant sedimentation flux). Thus, the observation that the haze scale height differs from the gas scale height implies that particle production is occurring below 20 km, which is consistent with their being generated chiefly from lower order hydrocarbon ices (but not HCN ice) (Lyons *et al.* 1992).

Sagan and Chyba (1990) give an expression for the sedimentation velocity of particles in Triton's atmosphere as a function of particle size. Assuming a surface pressure of 14 μbar , an "equivalent isothermal temperature" of 43K (Gurrola *et al.* 1992) to characterize the variation of pressure with altitude, and a haze bulk density of 0.6 (Krasnopolsky *et al.* 1992), this expression gives a haze sedimentation mass flux of $5\text{--}6 \times 10^{-15} \text{ g cm}^{-2} \text{ s}^{-1}$ at the surface in region 10, which corresponds closely to the integrated production rate of $5 \times 10^{-15} \text{ g cm}^{-2} \text{ s}^{-1}$ given by Strobel *et al.* (1990) for Triton's summer hemisphere. (The production rate given for the winter hemisphere is a factor of two smaller.)

We will next consider the lifetime and possible condensation mechanism for the discrete clouds found at high latitudes in Triton's troposphere. Using the equation given by Sagan and Chyba (1990) for the sedimentation velocity, and a particle mass density of 1 g cm^{-3} , we find fall times to the surface from an altitude of 8 km of about 1.5 days for $1.5 \mu\text{m}$ particles and 1.5 weeks for $0.23 \mu\text{m}$ particles.

Using the coagulation kernel given by Turco *et al.* (1982), simplified by assuming monodisperse particle sizes, coagulation times are found to be about a month for small cloud particles and several years for large ones. Condensation times are critically dependent on the difference between ambient pressure and the saturation vapor pressure, neither of which is known well enough to yield useful limits.

The fact that the coagulation times are substantially longer than the fallout times may constitute further evidence that condensation is taking place, but it is not possible to discriminate between the two possible cloud particle size regimes by comparing growth and fallout times.

Nitrogen condensation can occur as a result of adiabatic cooling in regions of large scale upwelling, where the ambient atmosphere has a static stability that is not too far from adiabatic. On Triton, large scale upwelling can be expected in places undergoing sublimation, since sublimation increases the basal pressure of the atmosphere (Ingersoll 1990). If this process is the source of the bright condensation clouds seen on the Voyager images, then active sublimation was occurring chiefly poleward of 30°S at the time of the Voyager flyby.

Alternatively, nitrogen condensation may have occurred in rapidly rising thermal plumes associated with local hot spots of "bare" ground (surface areas totally free of nitrogen ice), where local temperatures are not buffered by nitrogen phase changes (Ingersoll and Tryka 1990). Bare ground spots with low albedos and near the subsolar latitude (45°S at the time of the Voyager flyby) had temperatures significantly in excess of the temperature of nitrogen ice covered surfaces. In this model, rapidly ascending air cools adiabatically and condensation occurs almost independent of the background static stability when the rising gas reaches the local frost point temperature. If this mechanism is the source of the bright condensation clouds, then some or much of the surface poleward of 30°S was denuded of nitrogen frost at the time of the Voyager flyby, as suggested by some models of the seasonal cycle of nitrogen (Spencer and Moore 1992).

Still a third mechanism for producing nitrogen condensation clouds is one that may be related to plume generation. In this case, a high nitrogen pressure is generated in the subsurface and is released at surface vents (e.g. Brown *et al.* 1990). Once again, rapidly rising motions lead to nitrogen condensation. Geysers were detected at high southern latitudes, not too far from the subsolar latitude (Soderblom *et al.* 1990). The conditions for their formation may include both high solar insolation and the availability of nitrogen ice at and close to the surface (Brown *et al.* 1990). If so, the observed spatial distribution of the bright condensation clouds seen on the satellite's limb is consistent with the presence of nitrogen ice on the surface at a number of places poleward of 30°S .

It may be possible to distinguish among these alternative ways of making nitrogen condensation clouds on the basis of the observed vertical distribution of the bright cloud material. According to Stansberry *et al.* (1992), the air above local hot spots will be heated to temperatures of $\sim 3\text{--}10\text{ K}$ higher than the frost point of nitrogen at the surface. The adiabatic lapse rate on Triton is about 0.75 K/km , so air rising in a thermal plume does not begin condensing until it reaches altitudes of 4 to 15 km; i.e. no condensation is expected close to the surface. But the high resolution limb images of Pollack *et al.* (1990) clearly show bright cloud material present all the way down to the surface. Therefore, the bright condensation clouds are probably not produced by thermal plumes generated over bare ground, and nitrogen ice was widely present poleward of 30°S at the time of the Voyager flyby. Both the remaining mechanisms — large scale rising motion induced by sublimation and plume genesis — may play roles in producing the condensation clouds. The widespread presence of these clouds suggest a large scale source, while the shape of some discrete clouds suggest a local source (Pollack *et al.* 1990).

Nitrogen is the major constituent of Triton's atmosphere, and its ambient pressure is essentially the same everywhere on Triton. Assuming that the clouds are composed of condensed N_2 , the fact that they appear preferentially toward the south pole indicates systematically lower atmospheric temperatures there, despite the fact that solar insolation is currently

highest at high southern latitudes. This is also consistent with the latitudinal temperature gradient required to produce west winds at 8 km from the thermal wind equation (Ingersoll 1990). A frost covered surface would be relatively cold, so an increase in condensation clouds toward the pole is compatible with a frost covered polar cap. Some of the frost free models of Spencer and Moore (1992) have surface temperatures which decrease monotonically between the equator and 60-70°S. To the extent that surface temperatures on Triton can be correlated with atmospheric temperatures, this would also be consistent with increased N₂ condensation at higher southern latitudes. However, as stated in the previous paragraph, these models have difficulty generating clouds which extend all the way down to the surface.

The latent heat released by the condensation of our N₂ clouds near the tropopause corresponds to an upward heat flux of $\sim 0.01 \text{ erg cm}^{-2} \text{ s}^{-1}$ for the $\sim 0.25 \text{ }\mu\text{m}$ particles, or to $\sim 1 \text{ erg cm}^{-2} \text{ s}^{-1}$ for the $\sim 1.5 \text{ }\mu\text{m}$ particles. This compares to an estimated upward flux due to turbulent transport of $\sim 5 \text{ erg cm}^{-2} \text{ s}^{-1}$ (Stansberry *et al.* 1992), and to a downward flux due to conduction from the ionosphere of $\sim 1.15 \times 10^{-3} \text{ erg cm}^{-2} \text{ s}^{-1}$ (Yelle *et al.* 1991). Latent heat release can therefore be a significant component of the total energy flux on Triton.

Acknowledgements

We thank Floyd Herbert for enlightening discussions of the Voyager UVS results. This work was supported by NASA under RTOP 889-59-01-28 of the Neptune Data Analysis Program.

References

- BROADFOOT, A.L., S.K. ATREYA, J.L. BERTAUX, J.E. BLAMONT, A.J. DESSLER, T.M. DONAHUE, W.T. FORRESTER, D.T. HALL, F. HERBERT, J.B. HOLBERG, D.M. HUNTEN, V.A. KRASNOPOLSKY, S. LINICK, J.I. LUNINE, J.C. MCCONNELL, H.W. MOOS, B.R. SANDEL, N.M. SCHNEIDER, D.E. SHEMANSKY, G.R. SMITH, D.F. STROBEL, AND R.V. YELLE 1989. Ultraviolet Spectrometer Observations of Neptune and Triton. *Science* **246**, 1459-1466.
- BROWN, R.H., R.L. KIRK, T.V. JOHNSON, AND L.A. SODERBLOM 1990. Energy sources for Triton's geyser-like plumes. *Science* **250**, 431-435.
- CRUIKSHANK, D.P., R.H. BROWN, AND R.N. CLARK 1984. Nitrogen on Triton. *Icarus* **58**, 293-305.
- CRUIKSHANK, D.P., R.H. BROWN, L.P. GIVER, AND A.T. TOKUNAGA 1989. Triton: Do we see the surface?. *Science* **245**, 283-286.
- DANIELSON, G.E., P.N. KUPFERMAN, T.V. JOHNSON, AND L.A. SODERBLOM 1981. Radiometric performance of the Voyager cameras. *J. Geophys. Res.* **86**, 8683-8689.
- GURROLA, E.M., E.A. MAROUF, V.R. ESHLEMAN, G.L. TYLER, AND P.A. ROSEN 1992. Analysis of Voyager radio occultation observations of Triton. *Neptune and Triton Conference Proceedings*, Tucson, Arizona, January 1992, pp. 28.
- HANSEN, J.E., AND J.W. HOVENIER 1974. Interpretation of the polarization of Venus. *J. Atmos. Sci.* **31**, 1137-1159.
- HILLIER, J.K., P. HELFENSTEIN, A. VERBISCHER, AND J. VEVERKA 1991. Voyager photometry of Triton: Haze and surface photometric properties. *J. Geophys. Res.* **96**, 19,203-19,209.
- INGERSOLL, A.P. 1990. Dynamics of Triton's atmosphere. *Nature* **344**, 315-317.

- INGERSOLL, A.P., AND K.A. TRYKA 1990. Triton's plumes: the dust devil hypothesis. *Science* **250**, 435-437.
- KRASNOPOLSKY, V.A., B.R. SANDEL, AND F. HERBERT 1992. Properties of haze in the atmosphere of Triton. *J. Geophys. Res.* in press.
- LYONS, J.R.L., Y.L. YUNG, AND M. ALLEN 1992. Solar Control of the Upper Atmosphere of Triton. *Science* **256**, 204-206.
- MCEWEN, A.S. 1990. Global color and albedo variations on Triton. *Geophys. Res. Lett.* **17**, 1765-1768.
- POLLACK, J.B., K. RAGES, S.K. POPE, M.G. TOMASKO, P.N. ROMANI, AND S.K. ATREYA 1987. Nature of the stratospheric haze on Uranus: Evidence for condensed hydrocarbons. *J. Geophys. Res.* **92**, 15,037-15,065.
- POLLACK, J.B., J.M. SCHWARTZ, AND K. RAGES 1990. Scatterers in Triton's atmosphere: Implications for the seasonal volatile cycle. *Science* **250**, 440-443.
- RAGES, K., AND J.B. POLLACK 1983. Vertical distribution of scattering hazes in Titan's upper atmosphere. *Icarus* **55**, 50-62.
- SAGAN, C., AND C. CHYBA 1990. Triton's streaks as windblown dust. *Nature* **346**, 546-548.
- SMITH, B.A., L.A. SODERBLOM, D. BANFIELD, C. BARNET, A.T. BASILEVSKY, R.F. BEEBE, K. BOLLINGER, J.M. BOYCE, A. BRAHIC, G.A. BRIGGS, R.H. BROWN, C. CHYBA, S.A. COLLINS, T. COLVIN, A.F. COOK II, D. CRISP, S.K. CROFT, D. CRUIKSHANK, J.N. CUZZI, G.E. DANIELSON, M.E. DAVIES, E. DE JONG, L. DONES, D. GODFREY, J. GOGUEN, I. GRENIER, V.R. HAEMMERLE, H. HAMMEL, C.J. HANSEN, C.P. HELFENSTEIN, C. HOWELL, G.E. HUNT, A.P. INGERSOLL, T.V. JOHNSON, J. KARGEL, R. KIRK, D.I. KUEHN, S. LIMAYE, H. MASURSKY, A. MCEWEN, D. MORRISON, T. OWEN, W. OWEN, J.B. POLLACK, C.C. PORCO, K. RAGES, P. ROGERS,

- D. RUDY, C. SAGAN, J. SCHWARTZ, E.M. SHOEMAKER, M. SHOWALTER, B. SICARDY, D. SIMONELLI, J. SPENCER, L.A. SROMOVSKY, C. STOKER, R.G. STROM, V.E. SUOMI, S. P. SYNOTT, R.J. TERRILE, P. THOMAS, W.R. THOMPSON, A. VERBISER, AND J. VEVERKA 1989. Voyager 2 at Neptune: Imaging science results. *Science* **246**, 1422-1449.
- SODERBLOM, L.A., S.W. KIEFFER, T.L. BECKER, R.H. BROWN, A.F. COOK, II, C.J. HANSEN, T.V. JOHNSON, R.L. KIRK, AND E.M. SHOEMAKER 1990. Triton's geyser-like plumes: discovery and basic characterization. *Science* **250**, 410-415.
- SPENCER, J.R., AND J.M. MOORE 1992. The influence of thermal inertia on temperatures and frost stability on Triton. *Icarus*, in press.
- STANSBERRY, J.A., R.V. YELLE, J.I. LUNINE, AND A.S. MCEWAN 1992. Energy coupling between Triton's surface and atmosphere. *Icarus*, in press.
- STROBEL, D.F., M.E. SUMMERS, F. HERBERT, AND B.R. SANDEL 1990. The photochemistry of methane in the atmosphere of Triton. *Geophys. Res. Lett.* **17**, 1729-1732.
- THOMPSON, S.B., F. ARNOLD, R.B. SANDERSON, AND A.W. MANTZ 1973. Optical properties of cryodeposits on low scatter mirrors. *AIAA 8th Thermophysics Conference Proceedings*, Palm Springs, California, July 16-18 1973.
- TURCO, R.P., O.B. TOON, R.C. WHITTEN, R.G. KEESEE, AND D. HOLLENBACH 1982. Noctilucent clouds: Simulation studies of their genesis, properties and global influences. *Planet. Space Sci.* **30**, 1147-1181.
- TYLER, G.L., D.N. SWEETNAM, J.D. ANDERSON, S.E. BORUTZKI, J.K. CAMPBELL, V.R. ESHLEMAN, D.L. GRESH, E.M. GURROLA, D.P. HINSON, N. KAWASHIMA, E.R. KURSINSKI, G.S. LEVY, G.F. LINDAL, J.R. LYONS, E.A. MAROUF, P.A. ROSEN, R.A.

SIMPSON, AND G.E. WOOD 1989. Voyager radio science observations of Neptune and Triton. *Science* **246**, 1466-1473.

YELLE, R.V., J.I. LUNINE, AND D.M. HUNTEN 1991. Energy balance and plume dynamics in Triton's lower atmosphere. *Icarus* **89**, 347-358.

Table I: Description of Triton Images

FDS count	Camera and Filter ^a	Phase angle (°)	Resolution (km/p)
11398.11	WA-B	159.4	9.5
11398.17	WA-G	157.8	10.1
11398.23	WA-V	156.2	10.6
11398.29	WA-B	154.8	11.2
11398.35	WA-G	153.6	11.7
11398.56	WA-V	150.0	12.7
11399.07	WA-G	148.5	14.8
11399.18	WA-B	147.1	15.9
11399.29	WA-O	146.1	17.0
11399.51	WA-B	144.2	19.1
11400.02	WA-G	143.4	20.2
11400.13	WA-V	142.7	21.4
11400.24	WA-B	142.1	22.4
11400.48	WA-O	140.9	24.8
11400.54	WA-G	140.6	25.4

^aEffective wavelengths of the filters on the Voyager 2 wide angle camera are:

V-0.431 μ m, B-0.474 μ m, G-0.562 μ m, O-0.596 μ m

Table II: Defining Characteristics of Atmospheric Models

<i>1-Component Models — Haze Only</i>	
<u>Case</u>	<u>Description</u>
a1)	Absorbing haze with phase function found using Mie theory
b1)	Conservatively scattering haze with phase function found using Mie theory
c1)	Conservatively scattering haze with Rayleigh phase function
<i>2-Component Models — Haze and Discrete Cloud</i>	
<u>Case</u>	<u>Description</u>
a2)	Large Mie scattering cloud particles ($r_c > 0.6 \mu\text{m}$) with optical depth ≤ 0.3
b2)	Small Mie scattering cloud particles ($r_c < 0.3 \mu\text{m}$) with optical depth ≤ 0.3
c2)	Small Mie scattering cloud particles with optical depth ≤ 0.1

Table III: Optimum Values of Free Parameters for 1-Component Models

Region	Case	r_h (μm)	n_h (10^8 cm^{-2})	H_h (km)	a_h	b_h (μm^{-1})	χ^2 /d.o.f.
1	a1)	0.150 ± 0.008	0.18 ± 0.05	5.5 ± 0.3	0 ± 5	2 ± 11	0.80
9	a1)	0.177 ± 0.016	0.031 ± 0.011	11.6 ± 0.6	-0.7 ± 0.4	1.6 ± 0.9	0.99
10	a1)	0.169 ± 0.014	0.026 ± 0.015	10.8 ± 0.6	0.05 ± 0.09	0.0	0.79
	b1)	0.173 ± 0.012	0.020 ± 0.006	11.0 ± 0.6	0.0	0.0	0.79
	c1)	0.025	3720 ± 140	10.8 ± 0.6	0.0	0.0	0.92

Table IV: Model Optical Depths

Region	Case	Vertical optical depth to surface			
		Violet	Blue	Green	Orange
1	a1)	0.028	0.028	0.027	0.026
	a2)	0.123	0.123	0.122	0.121
	b2)	0.041	0.042	0.044	0.044
2	a2)	0.308	0.306	0.302	0.303
	b2)	0.364	0.317	0.235	0.207
	c2)	0.111	0.099	0.081	0.075
3	a2)	0.368	0.364	0.359	0.363
	b2)	0.409	0.351	0.250	0.216
	c2)	0.118	0.104	0.083	0.077
4	a2)	0.371	0.366	0.366	0.372
	b2)	0.422	0.361	0.257	0.224
	c2)	0.121	0.104	0.077	0.068
5	a2)	0.350	0.358	0.353	0.346
	b2)	0.375	0.344	0.289	0.271
	c2)	0.112	0.101	0.085	0.080
6	a2)	0.361	0.355	0.330	0.319
	b2)	0.359	0.342	0.320	0.316
	c2)	0.106	0.101	0.098	0.098
7	a2)	0.352	0.354	0.340	0.331
	b2)	0.377	0.354	0.311	0.297
	c2)	0.111	0.104	0.096	0.093
8	a2)	0.337	0.337	0.336	0.336
	b2)	0.384	0.324	0.194	0.144
	c2)	0.100	0.096	0.088	0.084
9	a1)	0.0068	0.0062	0.0057	0.0057
	a2)	0.134	0.135	0.135	0.135
	b2)	0.327	0.262	0.164	0.135
	c2)	0.090	0.089	0.087	0.085
10	a1)	0.0049	0.0042	0.0032	0.0028
	b1)	0.0039	0.0033	0.0023	0.0020
	c1)	0.0143	0.0100	0.0050	0.0039

Table V: Optimum Values of Free Parameters for 2-Component Models

Region	Case	r_c (μm)	n_c (10^6cm^{-2})	l_c (km)	n_h (10^6cm^{-2})	l_h (km)	a_c	b_c (μm^{-1})	χ^2 /d.o.f.
1	a2)	1.68 ± 0.14	0.6 ± 0.2	1.0 ± 0.2	1.43 ± 0.07	7.0 ± 0.5	-0.019 ± 0.010	0.07 ± 0.02	0.54
	b2)	0.167 ± 0.006	27 ± 6	2.0 ± 0.3	1.26 ± 0.07	7.8 ± 0.5	-0.4 ± 0.9	1.6 ± 1.7	0.58
2	a2)	1.55 ± 0.06	1.8 ± 0.6	16 ± 37	1.77 ± 0.14	10.2 ± 0.9	-0.029 ± 0.005	0.069 ± 0.011	1.28
	b2)	0.205 ± 0.006	200 ± 20	8 ± 2	1.62 ± 0.15	11.2 ± 1.1	0.14 ± 0.02	-0.15 ± 0.04	1.38
	c2)	0.198 ± 0.012	67 ± 15	16 ± 19	0.9 ± 0.2	14 ± 4	0.03 ± 0.05	0.10 ± 0.11	4.76
3	a2)	1.49 ± 0.07	2.3 ± 0.2	16 ± 10	2.24 ± 0.17	9.3 ± 0.8	-0.028 ± 0.003	0.064 ± 0.007	1.67
	b2)	0.209 ± 0.005	221 ± 19	16 ± 9	2.21 ± 0.19	9.9 ± 0.9	0.125 ± 0.014	-0.15 ± 0.03	1.71
	c2)	0.192 ± 0.011	90 ± 20	16 ± 21	0.8 ± 0.3	14 ± 6	-0.01 ± 0.04	0.12 ± 0.09	8.27
4	a2)	1.42 ± 0.06	2.5 ± 0.2	16 ± 12	3.2 ± 0.2	8.7 ± 0.7	-0.030 ± 0.003	0.071 ± 0.006	2.06
	b2)	0.214 ± 0.004	214 ± 16	16 ± 11	3.3 ± 0.3	9.0 ± 0.7	0.108 ± 0.013	-0.13 ± 0.03	2.06
	c2)	0.205 ± 0.009	76 ± 14	16 ± 21	1.1 ± 0.4	14 ± 5	0.02 ± 0.03	0.01 ± 0.07	8.95
5	a2)	0.727 ± 0.012	7.1 ± 0.4	16 ± 13	3.96 ± 0.19	8.9 ± 0.5	-0.058 ± 0.009	0.18 ± 0.02	1.22
	b2)	0.258 ± 0.004	95 ± 6	16 ± 13	4.6 ± 0.2	8.6 ± 0.5	0.10 ± 0.03	0.03 ± 0.06	1.28
	c2)	0.252 ± 0.007	31 ± 3	16 ± 21	2.6 ± 0.4	11.2 ± 1.6	0.00 ± 0.05	0.16 ± 0.12	4.31
6	a2)	0.675 ± 0.010	8.3 ± 0.4	16 ± 14	3.79 ± 0.17	8.9 ± 0.4	-0.124 ± 0.014	0.34 ± 0.03	1.16
	b2)	0.283 ± 0.004	69 ± 5	16 ± 14	4.6 ± 0.2	8.4 ± 0.4	-0.14 ± 0.07	0.62 ± 0.14	1.33
	c2)	0.284 ± 0.008	20.0 ± 1.7	16 ± 22	3.1 ± 0.4	9.9 ± 1.1	-0.41 ± 0.12	1.1 ± 0.3	3.82
7	a2)	0.704 ± 0.012	7.7 ± 0.4	16 ± 15	3.7 ± 0.2	9.9 ± 0.6	-0.080 ± 0.013	0.25 ± 0.03	1.70
	b2)	0.259 ± 0.004	90 ± 6	16 ± 15	4.5 ± 0.3	9.4 ± 0.5	0.13 ± 0.06	0.07 ± 0.12	1.68
	c2)	0.265 ± 0.008	25 ± 2	16 ± 24	2.9 ± 0.4	11.0 ± 1.4	-0.10 ± 0.10	0.5 ± 0.2	4.70
8	a2)	1.75 ± 0.08	1.52 ± 0.16	16 ± 21	2.71 ± 0.16	9.5 ± 0.6	-0.042 ± 0.008	0.124 ± 0.019	1.55
	b2)	0.156 ± 0.005	320 ± 60	16 ± 19	2.96 ± 0.18	9.4 ± 0.6	0.8 ± 0.2	-1.1 ± 0.4	1.39
	c2)	0.18 ± 0.02	48 ± 11	16 ± 26	2.3 ± 0.2	10.5 ± 1.1	0.4 ± 1.1	0.0 ± 1.2	2.66
9	a2)	2.072 ± 0.004	0.44 ± 0.03	16 ± 27	1.34 ± 0.08	11.1 ± 0.9	-0.104 ± 0.020	0.29 ± 0.05	0.77
	b2)	0.07 ± 0.02	8000 ± 10^4	16 ± 21	1.40 ± 0.07	11.5 ± 0.8	0.10 ± 0.11	-0.11 ± 0.13	0.57
	c2)	0.101 ± 0.003	199 ± 13	16 ± 24	1.33 ± 0.09	11.4 ± 0.9	0.0 ± 0.2	0.8 ± 0.6	0.71

Figure captions

1. This figure shows the locations of the data sets fit to the spherical shell atmospheric models. The location of Triton's limb in each of the green filter images is shown by the heavy lines, with the corresponding FDS numbers given in the legend. Each sheaf of thinner curved lines perpendicular to the limbs represents the radial limb scans taken from each of the 15 images, for each of ten labelled regions. These labels correspond to the region numbers in Tables III, IV, and V. Finally, the location of the surface terminator is shown (thin solid line), as well as the location where the sun drops below the horizon for an altitude of 10 km above the surface (thin dashed line). Note that for some regions the limb scans cover more than 30° in latitude, which makes it rather unlikely that the atmosphere is homogeneous throughout the region. The subsolar point is shown near 45°S , 355°E .
2. This is the complete data set for region 10, including the violet (three frames), orange (two frames), blue (four frames), and green (five frames) filter data, shown together with three possible model atmospheres: case *b1* — conservative scatterers with a mean particle radius of $0.19^{+0.02}_{-0.01} \mu\text{m}$ (solid line), case *a1* — absorbing particles with a mean radius of $0.18^{+0.02}_{-0.01} \mu\text{m}$ (dashed line generally indistinguishable from solid line), and case *c1* — Rayleigh scatterers (dotted line). ϕ is the solar phase angle at the center of Triton's disk in each image.
3. This is the complete data set for region 3, including the violet (three frames), orange (two frames), blue (five frames), and green (five frames) filter data. Three model atmospheres are shown: case *a2* — ≈ 0.3 optical depths of $1.5 \mu\text{m}$ particles (solid line), case *b2* — ≈ 0.3 optical depths of $0.22 \mu\text{m}$ particles (dashed line), and case *c2* — ≈ 0.1 optical depths of $0.20 \mu\text{m}$ particles (dotted line). Case *c2* fits the data much less well than the other two.

4. Albedo weighted single scattering phase function between 0° and 50° scattering angle, for cases *a2* (solid line) and *b2* (dashed line) from Fig. 3, for a) violet filter, b) blue filter, c) green filter, and d) orange filter. The scattering angles of the Voyager observations are shown as vertical lines
5. This is the complete data set for region 6, with the same layout as Fig. 3. This is an example of an "ill behaved" region, since many of the limb scans contain humps at radii less than 1350 km, which cannot possibly be fit by any horizontally homogeneous atmosphere, even if the condition of an exponential extinction profile is relaxed. The points shown as open circles were not included in the least-squares fitting procedure.
6. The location of all the points in all the radial scans for which I/F was clearly affected by local inhomogeneities (most likely local increases in the optical depth) in the cloud properties. The size of each dot crudely corresponds to the amount by which I/F deviated from its "background" value. The location of two plumes seen in the highest resolution images of the surface are marked by \times 's, and the location of a haze free area noted by Pollack *et al.* (1990) is shown as a dashed ellipse. The subsolar point is also shown, at 45°S , 357°E .

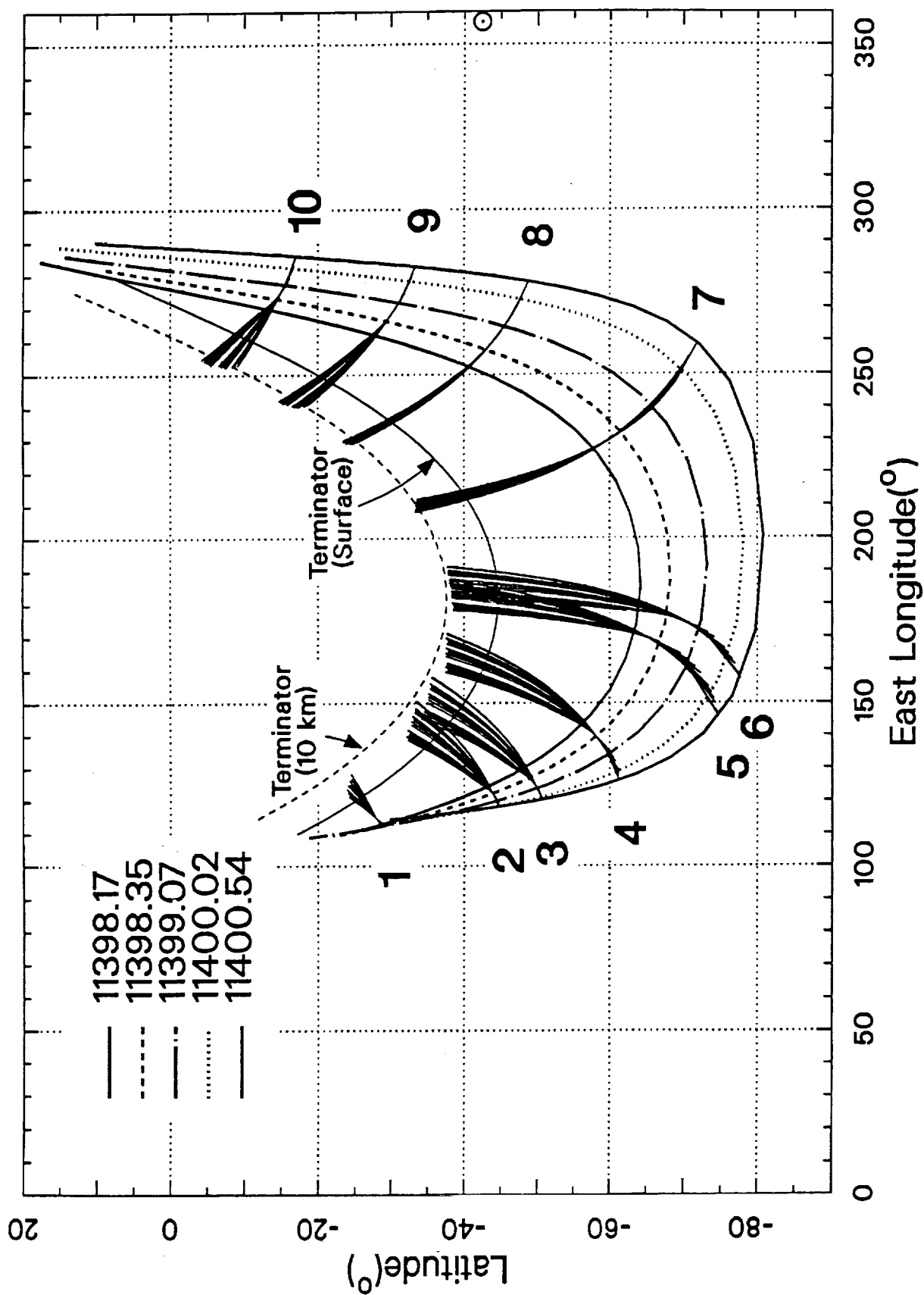
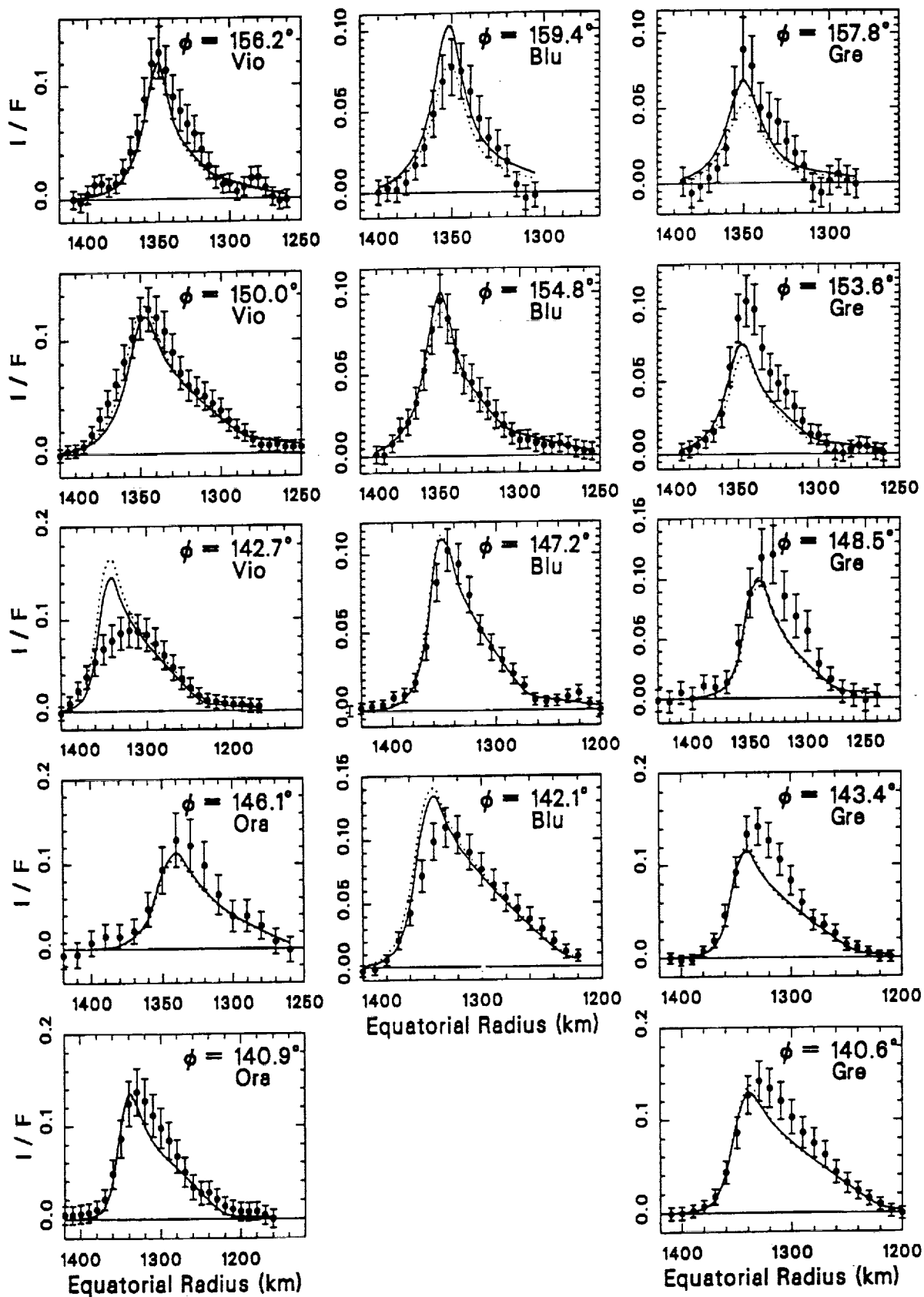
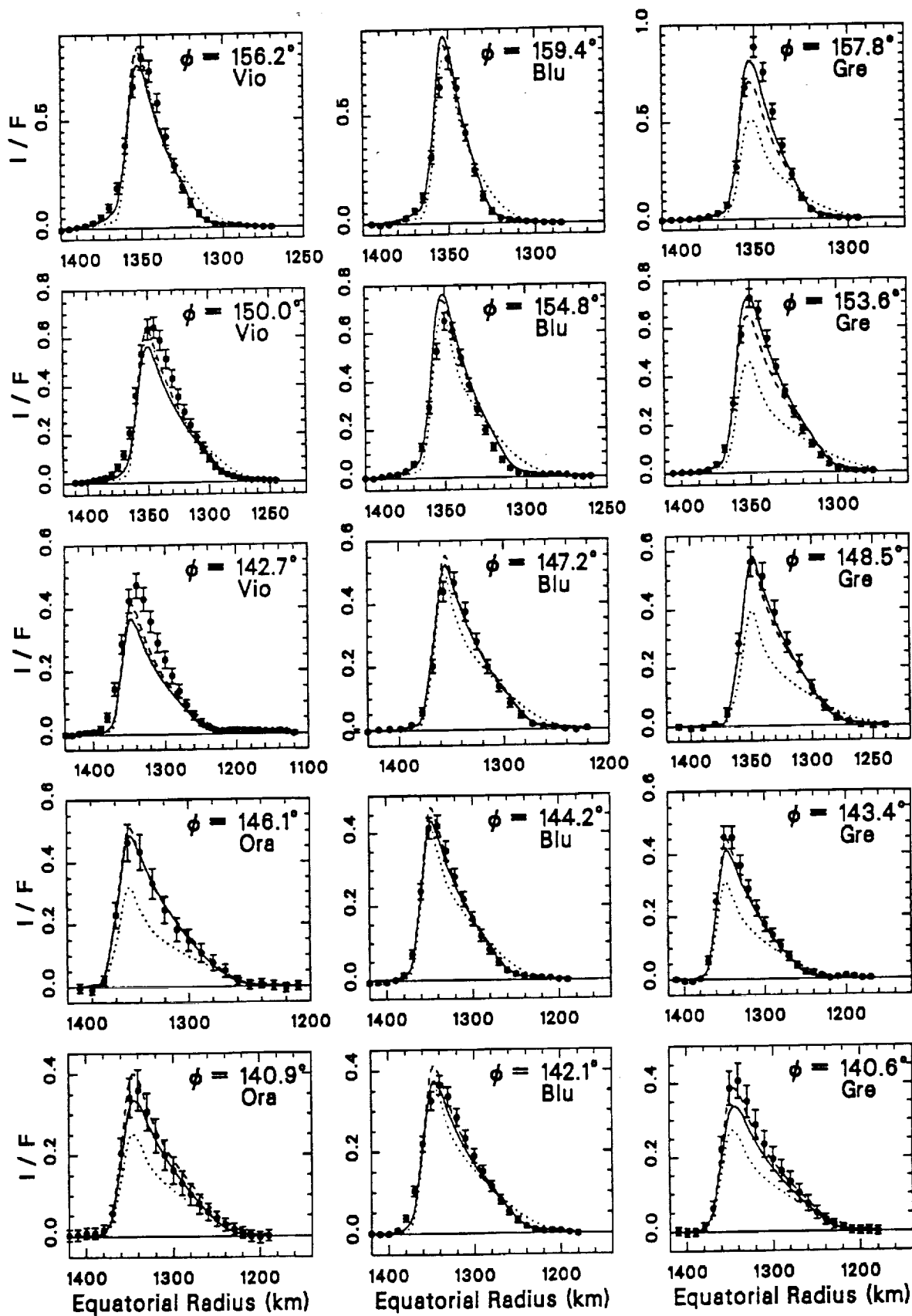
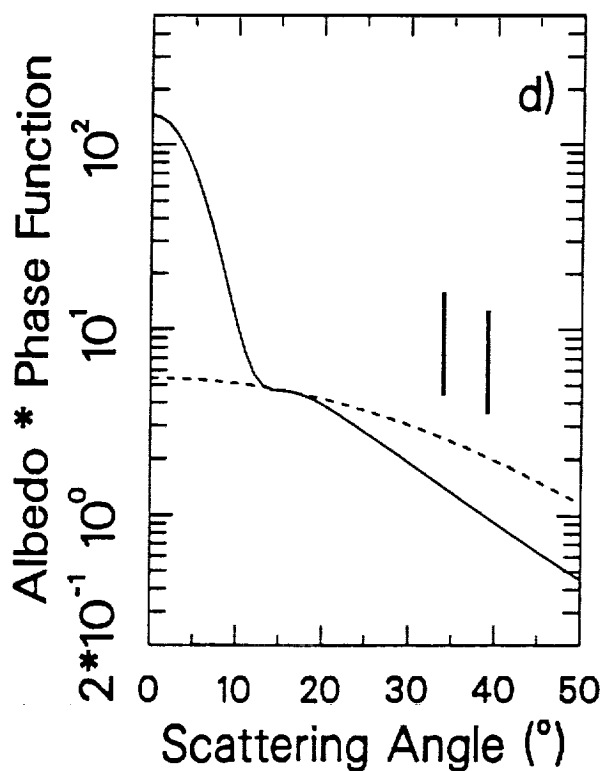
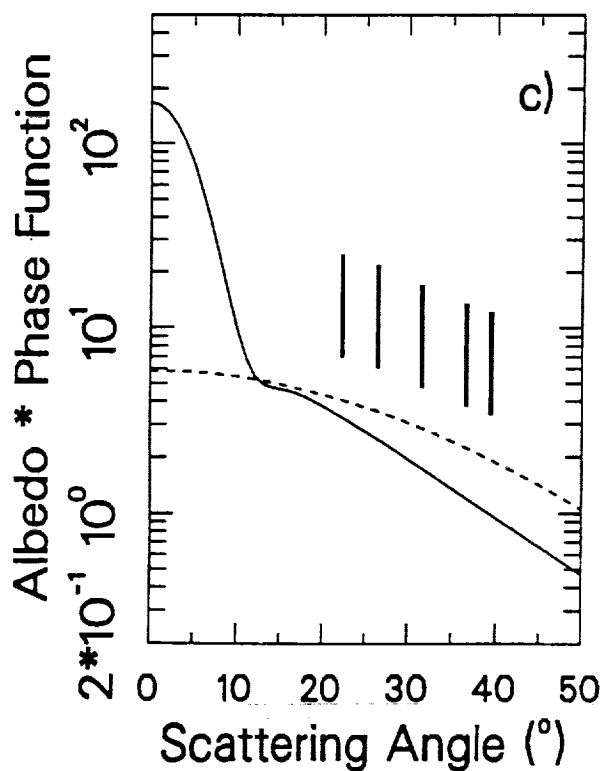
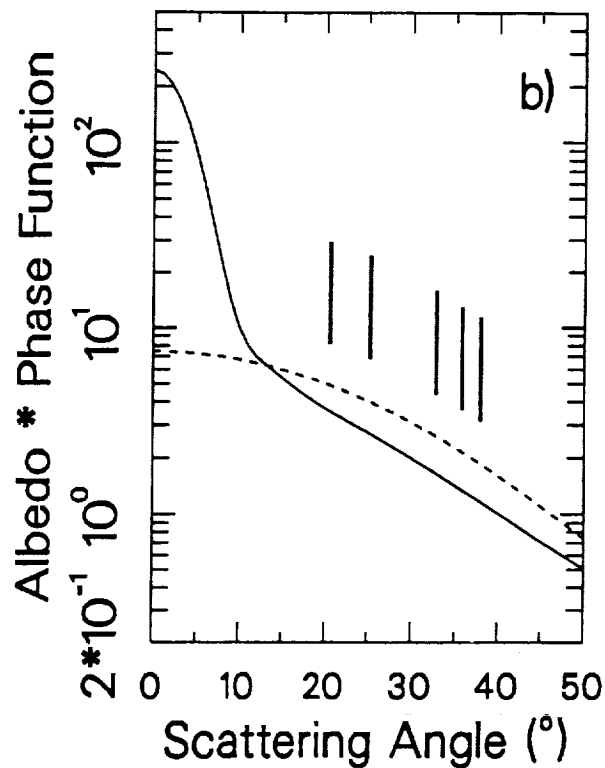
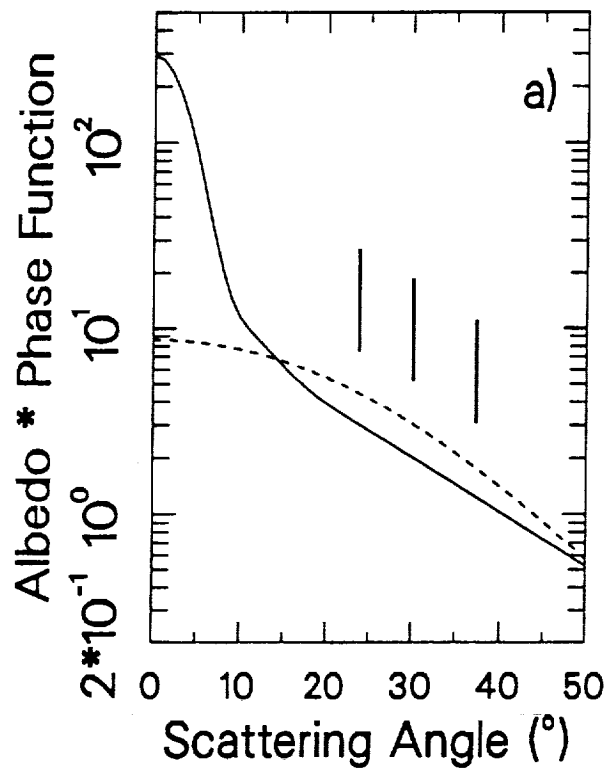
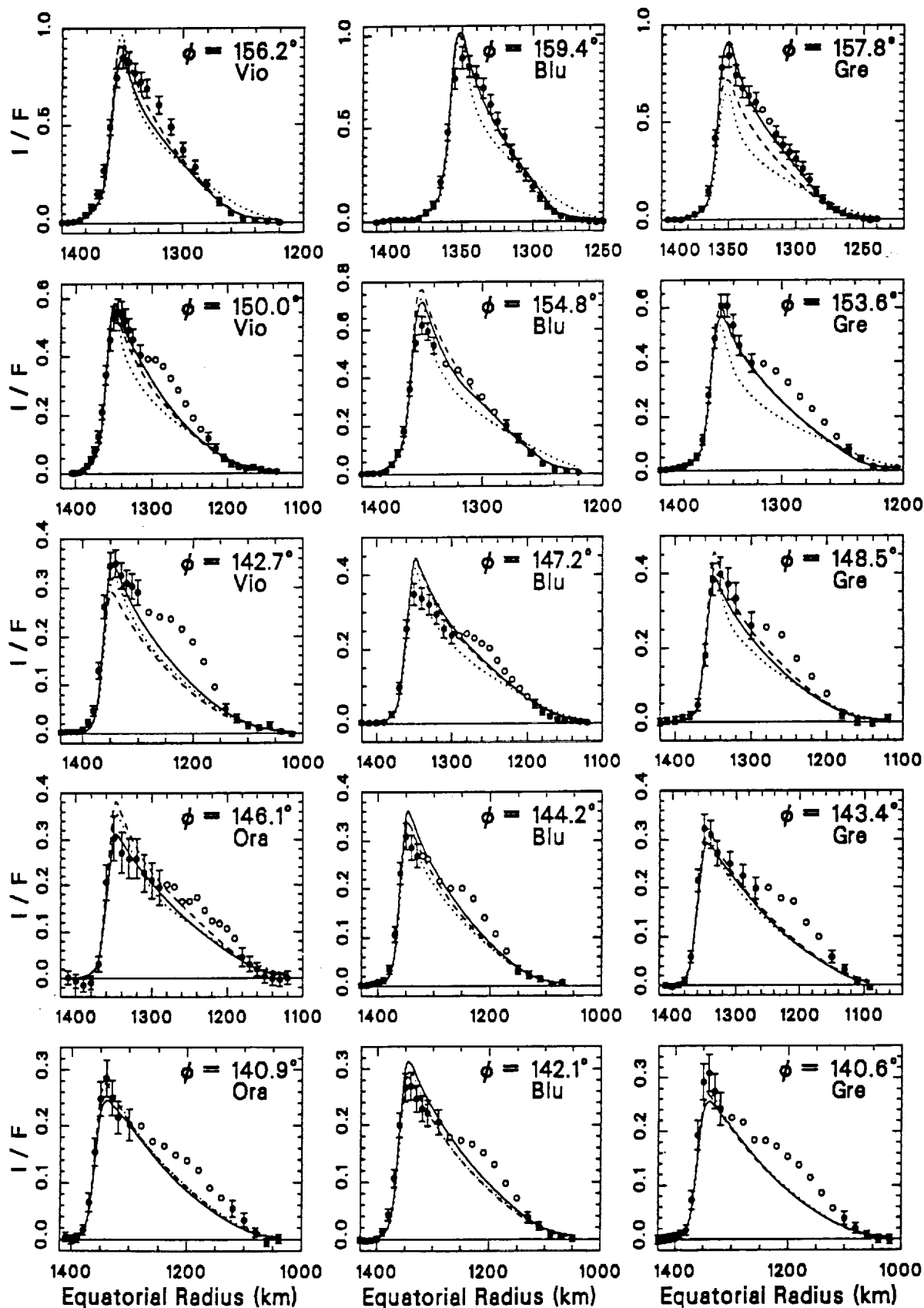


Fig. 1
Rages and Pollack









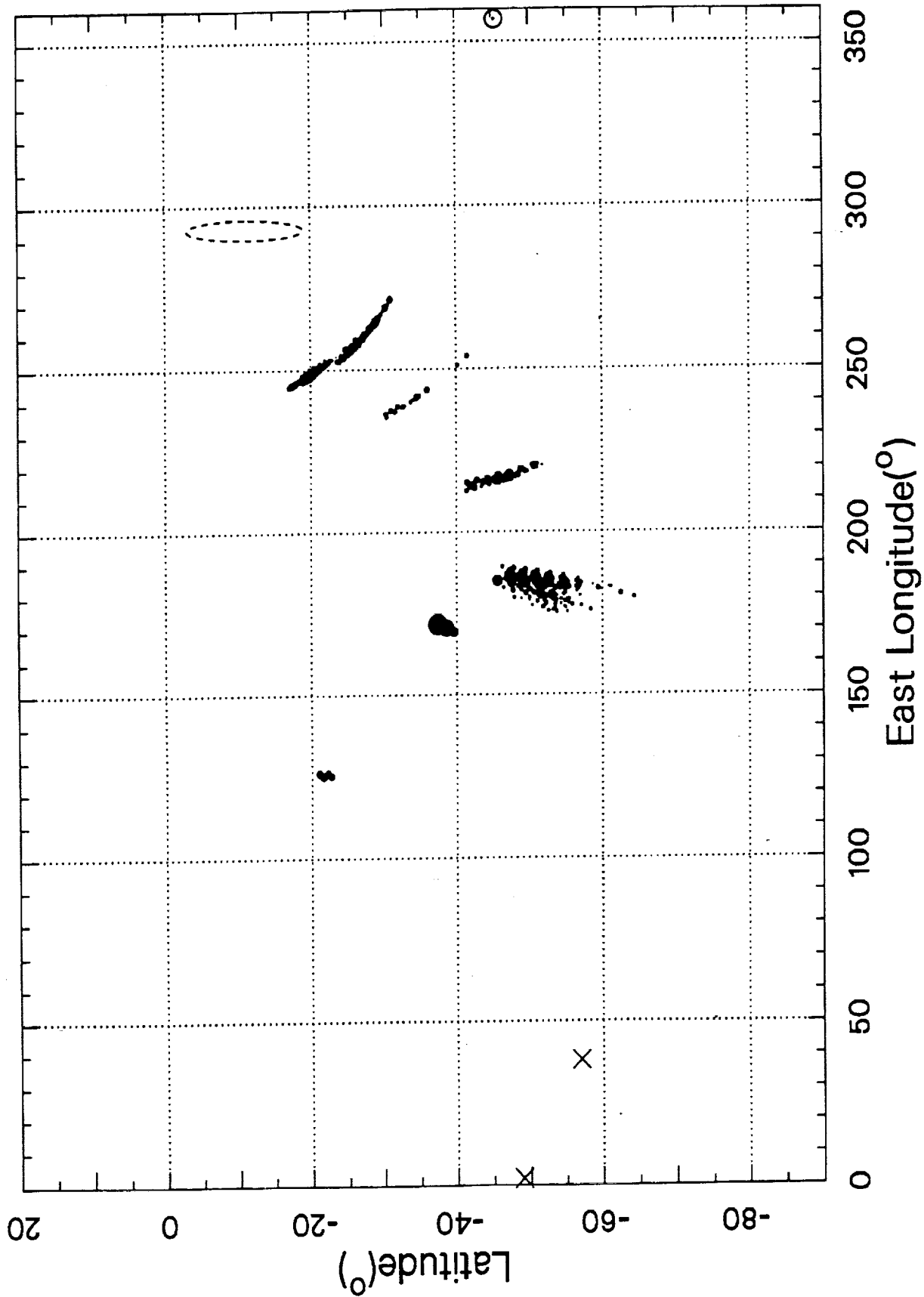


Fig. 6
Rages and Pollack